High energy charge, antioxidant capacity, and amino acid contents are conserved features of T cell metabolism

Samantha O'Keeffe[1], Harin Sim[2], Elle McCue[3], Junyoung O. Park[1,2]*

[1] Department of Chemical and Biomolecular Engineering, University of California, Los Angeles, Los Angeles, CA 90095, USA

[2] Department of Bioengineering, University of California, Los Angeles, Los Angeles, CA 90095, USA

[3] Department of Mechanical and Aerospace Engineering, University of California, Los Angeles, Los Angeles, CA 90095, USA

* Correspondence to J.O.P. (jop@ucla.edu)

Abstract

T cell diversity and differentiation define individual adaptive immunity. Metabolism fuels adaptive immunity by driving proliferation, differentiation, and activation; however, how individual and lineage differences shape T cell metabolism remains unknown. Here we develop an ensemble method for absolute metabolome quantitation and quantify 84 metabolites in human primary T cells. Liquid chromatography-mass spectrometry of metabolites co-extracted from T cells and ^{13}C-labeled reference cells reveals absolute concentrations *en masse*. Across subtypes and individuals, T cell metabolomes resemble one another. T cells possess thermodynamically forward-driven glycolysis, high adenylate energy charge, large amino acid pools, and favorable redox ratios for anabolism and antioxidant defense. Across metabolism, metabolite concentrations exceed their associated Michaelis constants and inhibitor constants two thirds and half of the time, respectively. The conserved features of T cell metabolomes underlie a design principle: metabolite levels prime T cells for increased energy demand, oxidative stress, and rapid regulation that accompany immune response.

Individual variations in the immune system give rise to different levels of protection against diseases and have implications for developing immunotherapy[1-3]. In the context of T cells in adaptive immunity, individual variations arise from genetic diversity[4], T cell receptor (TCR) diversity[5], and differentiation into subtypes[6]. Since metabolism converts nutrients into usable energy and biochemical building blocks necessary for T cell differentiation, proliferation, and function[7-10], a fundamental question arises: how do T cell diversity and differentiation manifest in metabolism?

T cells are maintained in a quiescent state through tightly regulated metabolic processes[11] to promote survival and proliferation without activation[12]. T cell metabolism is reprogrammed in response to antigen stimulation[13] and sometimes mere expression of surface proteins such as chimeric antigen receptors (CARs) [14]. Among broad changes, energy generation shifts from oxidative phosphorylation to aerobic glycolysis, amino acid uptake increases, and overflow metabolism commences[14,15]. Such metabolic reprogramming brings about an increased supply of ATP, amino acids, and nucleotides for effective immune response on one hand[15], and increased reactive oxygen species (ROS)[16,17] and altered redox homeostasis that contribute to exhaustion and autoimmune disease pathogenesis on the other hand[18,19]. These prior findings paint relative changes in T cell metabolism as immune biomarkers and therapeutic targets[10,11]; however, a baseline metabolic profile of T cells is necessary to establish a solid foundation for mechanistic understanding and rational tuning of the adaptive immune system.

Absolute metabolite concentrations dictate cell physiology (e.g., signaling and osmolarity) and metabolic rates through Michaelis-Menten kinetics (**Eqn. 1**) and thermodynamics (**Eqn. 2**). For a reaction of the form S⇌P, its rate is described by the reversible Michaelis-Menten equation:

$$v = v_{max} \frac{[S]/K_{m,s}}{1+[S]/K_{m,s}+[P]/K_{m,p}} \left(1 - e^{\Delta G/RT}\right) \qquad \text{... Equation 1}$$

v_{max} is the maximum reaction rate, [S] and [P] are the concentrations of substrate S and product P, $K_{m,s}$ and $K_{m,p}$ are the Michaelis constants for S and P, R is the gas constant in J mol^{-1} K^{-1}, T is the temperature in Kelvins, and ΔG the Gibbs free energy of the reaction. ΔG is modified from its value at biochemical standard conditions (ΔG°') to account for the effect of metabolite concentrations:

$$\Delta G = \Delta G^{\circ\prime} + RT \ln \frac{[P]}{[S]} \qquad \text{... Equation 2}$$

Cells regulate metabolite levels to efficiently utilize metabolic networks and avoid toxic buildup[20]. In turn, metabolites shape metabolic activity by acting as substrates, products, and effectors[21-24]. The value of absolute metabolite concentrations warrants comprehensive metabolome quantitation in T cells.

Liquid chromatography-mass spectrometry (LC-MS) has been a workhorse in metabolomics[25]. Challenges in quantifying absolute metabolite concentrations in human T cells are twofold: *i*) biologically, primary T cell availability is limited for each individual; and *ii*) analytically, current detection tools have varying response factors (signal-to-quantity ratios) for different metabolites. To address the latter analytical challenge, cellular metabolites are spiked with known concentrations of internal standards. Stable isotopes such as ^{13}C are used to distinguish between intracellular metabolites and internal standards (**Fig. 1a**). Known concentrations of internal standards and LC-MS measurement of labeled-to-unlabeled isotope ratios for individual metabolites reveal their absolute concentrations[26,27]. The present isotope ratio-based

approach, while effective for a handful of metabolites or for immortalized cell lines, does not overcome the dual challenges of comprehensive absolute metabolome quantitation in human primary T cells.

To address these challenges, we developed an ensemble metabolite quantitation method for absolute quantitation of metabolite concentrations in human primary T cells. The ensemble method leverages the known metabolite concentrations in model systems including *E. coli* and immortalized mammalian cells[24] as internal reference. The reference cells were grown on uniformly ^{13}C-labeled glucose, [U-$^{13}C_6$]glucose, and co-extracted with T cells whose metabolite concentrations had been unknown (**Fig. 1b**). The known concentrations of metabolites in the reference cell and LC-MS measurement of labeled-to-unlabeled isotope ratios revealed absolute metabolite concentrations *en masse* (**Fig. 1c**).

Using the ensemble method, we quantified the absolute concentrations of 84 metabolites totaling 131-154 mM and 221 mM in human primary T cells and Jurkat cells, respectively. To our surprise, absolute metabolite concentrations displayed a strong resemblance across subtypes and individuals. Amino acids were the largest class of metabolites in T cells with glutamate and aspartate being the most abundant metabolite in Jurkat cells and primary T cells, respectively. The energy status of T cells was healthy with a high adenylate energy charge of 0.95 and favorable redox ratios $NADH/NAD^+ \approx 0.06$ and $NADPH/NADP^+ \approx 19$. Thermodynamic analysis revealed that glycolysis and glutathione reductase were moderately to strongly forward driven with Gibbs free energy changes (ΔG) of −67 kJ/mol and −30 kJ/mol, respectively. Kinetic analysis revealed that T cell metabolomes facilitated efficient enzyme utilization and regulation. These findings pointed to a metabolic design principle: conserved metabolite levels prime T cells for energy generation, antioxidant activity, and efficient regulation. Thus, our ensemble quantitation established a reference human T cell metabolome and the healthy baseline state of T cell metabolism.

Results

Co-extraction enables absolute metabolome quantitation *en masse*

Absolute metabolite concentrations offer quantitative insights into metabolic regulation, energetics, and enzyme efficiency, but a demand for large numbers of cells and internal standards forbid their measurement in human primary cells . To overcome these challenges, we innovated absolute metabolome quantitation in primary human T cells that uses isotopically labeled cellular metabolites as internal standards by co-extracting metabolites from the cells of interest (COI) and ^{13}C-labeled reference cells (REF). For each metabolite, ^{12}C-dominant peaks and ^{13}C-dominant ions were divided into unlabeled and labeled groups to account for ^{12}C impurities and natural ^{13}C abundance (**Fig. 1d**). During co-extraction, two cell types were kept separate to prevent unwanted interactions and perturbations until they were quenched (**Fig. 1b**). By using reference cells with known concentrations[24], the co-extraction method obviated the need for individual standards and parallelized absolute quantitation of multiple metabolites in a single sample.

To validate our approach, we performed co-extraction with known ratios of two cultures of *E. coli* grown on unlabeled or ^{13}C-labeled glucose in otherwise identical conditions (**Fig. 1e**). LC-MS analysis revealed the ratios of unlabeled to ^{13}C-labeled metabolites (U:L ratio) as expected from the ratios of extracted culture volumes (**Fig. 1f**). At all ratios tested (U:L ratio equal to 1:1, 4:1, and 20:1), the measurements globally stayed near the expected ratio with R^2=0.85, R^2=0.78, and R^2=0.67, respectively. However, the distributions of measured U:L ratios became broader as they deviated further from one due to the lower limit of

106 detection and ion suppression in the mass spectrometer (**Extended Data Fig. 1**). Since one-to-one ratios of
107 unlabeled to ^{13}C-labeled metabolites minimized variance and error, we tuned the U:L ratios to be near one
108 by co-extracting different amounts of the COI and the REF (**Fig. 1g**). Collectively, ^{13}C-labeling, judicious co-
109 extraction, and LC-MS enabled parallel quantification of metabolites from limited cells. In Jurkat T cells, we
110 quantified 68 metabolite concentrations, totaling 221 mM (**Fig. 1h**).

111 **Conservation of T cell metabolome across individuals**

112 We conducted absolute metabolome quantitation in human primary T cells from individual healthy donors.
113 To best capture *in vivo* T cell metabolism in two major T cell subtypes, we isolated $CD4^+$ and $CD8^+$ T cells by
114 negative selection from peripheral blood mononuclear cells (PBMCs) because ligand binding on cell surface
115 may affect cellular metabolism[14]. To allow T cells to reach homeostasis, we incubated them for two hours in
116 RPMI 1640 medium supplemented with 10% dialyzed fetal bovine serum. Within seven to nine hours of
117 blood collection, we extracted $CD4^+$ and $CD8^+$ T cell metabolites using the ensemble method (**Fig. 2a**). The
118 rapid extraction and measurement of T cell metabolome minimized the alteration of T cell proteome to
119 reveal *in vivo*-like T cell metabolism before it adapted to *in vitro* conditions.

120 We quantified 70 metabolites in $CD4^+$ and $CD8^+$ T cells from five donors (**Fig. 2b and Supplementary**
121 **Tables 1 and 2**). T cell metabolomes were highly correlated across the five donors tested (R^2>0.79) (**Fig.**
122 **2b**). While we did not obtain enough cells to quantify all 70 metabolites from all individual donors, the
123 resemblance across individuals revealed their integral parts in a consolidated picture of human T cell
124 metabolome. To account for individual variability and measurement uncertainty, we used weighted
125 bootstrapping (see **Methods**) for unifying metabolite measurements from five donors (**Fig. 3a and**
126 **Extended Data Fig. 2**). The total concentrations of measured metabolites spanning central carbon
127 metabolites, amino acids, nucleotides, redox metabolites, and others in $CD4^+$ and $CD8^+$ T cells were 154 mM
128 and 131 mM.

129 Amino acids represented the most abundant metabolite group comprising 73%, 67%, and 67% of the
130 measured metabolome in $CD4^+$, $CD8^+$, and Jurkat cells, respectively. The most abundant metabolite
131 measured in primary T cells was aspartate whereas in Jurkat cells glutamate was the most abundant.
132 Central carbon metabolites and nucleotides were the next most abundant groups, each comprising as much
133 as ~10% of the metabolome in primary T cells. Pyruvate and malate were consistently the most abundant
134 central carbon metabolites, and ATP and UTP were the most abundant nucleotides. Interestingly, 3-
135 phosphoserine and uridine were two of the most abundant metabolites measured in Jurkat cells, pointing
136 to the role of *de novo* serine[28] and pyrimidine[29] biosynthesis in T cell proliferation and development.

137 **Conservation of T cell metabolome across subtypes**

138 In addition to the broad resemblance between the metabolomes of T cell subtypes, we observed a near-
139 perfect correlation (R^2>0.95) between individual metabolite concentrations in $CD4^+$ and $CD8^+$ T cells (**Fig.**
140 **3b** and **Extended Data Fig. 3**). Despite some differences in some of the most abundant metabolites, as a
141 whole, metabolite concentrations in Jurkat cells were highly correlated with those of $CD4^+$ and $CD8^+$
142 primary T cells (R^2=0.88 and R^2=0.83). To assess if these correlations were noteworthy, we compared the
143 metabolomes of T cells to those of other systems (previously measured using the traditional isotope ratio-
144 based approach)[23,24]. Across subtypes and individuals, all correlations of T cell metabolite concentrations

had R^2 values of 0.8 or greater, exceeding those of other comparisons whose R^2 values ranged from 0.4 to 0.7 (**Fig. 3c**).

The lowest observed correlation was between T cells and *E. coli* with R^2 around 0.4 (**Extended Data Fig. 4a**). Most amino acid concentrations were higher in T cells, whereas the concentrations of select central carbon metabolites, nucleotides, and redox cofactors were higher in *E. coli*. The T cell metabolome showed a higher correlation (R^2>0.4) with yeast (*S. cerevisiae*) cells than with *E. coli* (**Extended Data Fig. 4b**). Both microbes possessed greater concentrations of glycolytic intermediates such as hexose phosphates, fructose-1,6-bisphosphate, and 3-phosphoglycerate. Metabolite concentrations in T cells were moderately correlated (R^2>0.6) with those of iBMK cells (**Extended Data Fig. 4c**). On one hand, the observed R^2 values across the kingdoms of life indicated a baseline conservation of metabolism beyond just its network structure. Between 40% and 65% of the variance in metabolite concentrations in human T cells could be accounted for by metabolite concentrations in disparate systems. On the other hand, the extraordinary conservation of the T cell metabolome across subtypes and individuals implied the existence of underlying design principles unique to T cell metabolism.

T cell metabolome conforms to Zipf's law

A recurring observation in metabolite profiles was the high abundance of select metabolites such as aspartate, glutamate, pyruvate, and ATP. Why do a few metabolites dominate the metabolome? To answer this question, we investigated whether metabolite concentrations followed Zipf's law (**Eqn. 3**), which states that, when measured values are sorted in decreasing order, the nth-ranked measurement f(n) is approximately inversely proportional to n.

$$f(n) \approx \frac{C}{n^{\alpha}} \qquad \text{... Equation 3}$$

where α and C represent fitted parameters that are approximately 1 and the highest (n=1) measured value, respectively.

We overlaid Zipf's law to ranked absolute metabolite concentrations such the fitted line goes through as many of the 95% confidence intervals of metabolite measurements as possible (see **Methods**). The top 35, 32, and 26 metabolites in $CD4^+$, $CD8^+$, and Jurkat cells followed Zipf's law (**Fig. 4a**). Zipf's law appears in many natural and artificial constructs (e.g., languages, city populations, and antibody nongenomic diversity[30]); however, the partial conformity of T cell metabolome to Zipf's law was news and suggestive of the completeness of our measurement of high abundance metabolites and the efficiency of the uneven distribution of the metabolite pool.

While the total metabolome pool size is bound by osmotics, the factors that affect the individual metabolite concentrations include metabolic network topology, reaction kinetics, and thermodynamics. We surmised that a metabolic network may operate more efficiently by concentrating metabolites positioned at highly interconnected nodes. Using a genome-scale reconstruction of human metabolism[31], we counted the number of metabolic reactions each metabolite is acting as a substrate or a product. Zipfian metabolites whose concentrations were high participated in more reactions than non-Zipfian metabolites with low concentrations. (**Fig. 4b**). While global cofactors such as ATP, NADH, and NADPH participated in numerous reactions regardless of their concentrations being high or low, we observed a modest correlation (R^2 as high as 0.3) between the connectivities and concentrations of non-cofactors (**Fig. 4c**). Aside from a few

184 cofactors (e.g., ATP and CoA), T cells did not keep large pools of cofactors, which require onerous
185 biosynthetic pathways, but instead recycled them since cofactors are not destroyed in the reactions that
186 they facilitate. Thus, metabolic network topology corroborated metabolite concentrations supporting
187 efficiency. While reaction kinetics and thermodynamics also shape the metabolome, a critical determinant
188 of a metabolite's concentration is its relevance to regulating biological functions beyond metabolism.
189 Aspartate, the most abundant metabolite in human primary T cells, is a central regulator of immune
190 function[32-37].

191 **T cells efficiently use and regulate enzymes**

192 Enzyme-catalyzed reactions display saturable kinetics with respect to metabolite concentrations (i.e.,
193 Michaelis-Menten kinetics). Non-dimensionalized concentration [met]/K_m, where [met] is the
194 concentration of a metabolite and K_m is the Michaelis constant for an enzyme active site with respect to the
195 metabolite, represents the occupancy of an enzyme active site: [met]/K_m ≥ 1 represents high occupancy
196 and efficient enzyme use whereas [met]/K_m < 1 represents low occupancy and inefficient enzyme use. We
197 observed that the distribution of non-dimensionalized concentrations (with true K_m) was significantly
198 narrower than the that with permutated K_m values as quantified by their interquartile ranges (IQRs) (**Fig.
199 5a**). The narrow distribution of non-dimensionalized concentrations suggested coevolution of enzymes and
200 metabolite concentrations toward efficient enzyme use.

201 Metabolites serve as both substrates and effectors for enzymes. As the substrate and the effector
202 increasingly occupy the active site and the effector binding site of an enzyme, their influences on the
203 reaction rate contract. Across all three T cell types, two thirds of substrate-enzyme pairs displayed
204 metabolite concentrations exceeding their corresponding K_m (**Fig. 5b and Supplementary Tables 3, 4,
205 and 5**). On the other hand, metabolites as inhibitors had their concentrations exceed the corresponding
206 dissociation constants of the enzyme-inhibitor complex (K_i) for half of inhibitor binding interactions (**Fig.
207 5c and Supplementary Tables 6, 7, and 8**). Accordingly, the distributions of log ratios of metabolite
208 concentrations to corresponding K_m values were left-skewed, whereas log ratios of metabolite
209 concentrations to corresponding K_i values appeared more symmetrical (**Extended Data Fig. 5**). In each of
210 the three T cell types, the former distribution of ln([met]/K_m) leaned to the right compared to the latter
211 distribution of ln([met]/K_i) (**Fig. 5d and Supplementary Table 9**). On the individual metabolite level, ATP
212 and glutathione saturated the majority of enzyme binding sites as either substrates or inhibitors, whereas
213 cyclic AMP and $NADP^+$ hardly occupied enzyme binding sites (**Extended Data Fig. 6**). Non-saturating
214 metabolites like cyclic AMP and $NADP^+$ influence reaction rates through mass action. On the other hand,
215 saturating metabolites like ATP and glutathione would have to decrease their concentrations drastically to
216 meaningfully influence reaction rates. Nonetheless, they may still influence reaction rates by modulating
217 ATP/ADP and GSH/GSSG ratios and shifting ΔG of near-equilibrium reactions[21,38]. The concentrations of
218 central carbon metabolites and purine nucleotides (excluding ATP) were distributed more evenly around
219 the respective K_m and K_i values, sensitizing reaction rates to changes in metabolite levels (presumably to
220 promote adaptation). Collectively, absolute metabolite concentrations manifested efficient utilization of
221 enzymes and modulation of enzyme activity.

222 **T cells maintain a high energy charge**

223 Absolute metabolite concentrations conferred energetic and thermodynamic insights into T cell
224 metabolism. ATP is the cellular energy currency. Exergonic ATP hydrolysis drives reactions, which are
225 otherwise thermodynamically unfavorable, and produces ADP in the process. Thus, maintaining a high
226 ATP-to-ADP ratio favors proper cellular function. In both primary and immortalized T cells, ATP/ADP
227 ratios were consistently high with an IQR of 16.8–20.3 (**Fig. 6a**), which is higher than those of other
228 eukaryotes yeast and iBMK cells (~3.95 and ~8.21, respectively)[24]. The high ATP/ADP ratio in resting T
229 cells may prime them for a rapid switch to proliferation and cytokine synthesis upon activation. To fully
230 account for cellular energetics, we quantified the adenylate energy charge (**Eqn. 4**), which reflects the total
231 energy stored in the adenylate pool.

232 $$Adenylate\ Energy\ Charge\ = \frac{[ATP] + {}^{1}/_{2}[ADP]}{[ATP] + [ADP] + [AMP]} \qquad \text{... Equation 4}$$

233 The adenylate energy charge was 0.93-0.96, tightly conserved across all T cell types (**Fig. 6b**). The observed
234 adenylate energy charge in T cells was at the very high end of the physiological range from 0.7 to 0.96 in
235 mammalian cells[24,39].

236 **T cells maintain favorable redox ratios**

237 Oxidative phosphorylation is the main source of ATP for aerobic organisms including humans. Using the
238 proton motive force generated by electron transport chain from electron donors such as NADH and $FADH_2$
239 to an electron acceptor O_2, oxidative phosphorylation drives ATP synthesis. The $NADH/NAD^+$ ratio in T
240 cells ranged from 0.04 to 0.08 (IQR) (**Fig. 6c**). The ATP/ADP and $NADH/NAD^+$ ratios affect the
241 thermodynamic driving force of glycolysis, which generates two ATP and two NADH molecules for each
242 glucose molecule (**Fig. 6d**). We determined the Gibbs free energy change (ΔG) across glycolysis to range
243 from −60 kJ/mol to −77 kJ/mol (**Fig. 6e and Supplementary Table 10**). Three quarters of Gibbs free
244 energy drop occurred in upper glycolysis (**Fig. 6f**). Thus, the low $NADH/NAD^+$ ratio played dual roles of
245 driving glycolysis forward (despite the high ATP/ADP) and preventing reactive oxygen species (ROS)
246 production.

247 Redox pairs also play a vital role of providing reducing power for scavenging ROS and anabolism.
248 Glutathione and NADPH are primary reducing agents in the cell. In T cells, glutathione plays a crucial role in
249 effector function[40]. T cells maintained a high ratio of antioxidant glutathione (GSH) to its oxidized
250 counterpart glutathione disulfide (GSSG) with the GSH/GSSG IQR ranging from 4 to 14 (**Fig. 6g**), which was
251 in line with healthy erythrocytes whose GSH/GSSG=5.88 (ref. [41]) but not as high as those observed in
252 human tissues[24,42] and whole blood[43]. For $NADPH/NADP^+$, we observed large variations, but they were
253 mostly high between 9 and 27 in T cells (**Fig. 6h**). Such variability was consistent with prior observations of
254 $NADPH/NADP^+$ of 2.30 in iBMK cells[24] and ~30 in immortalized mouse embryonic fibroblasts[44]. In addition
255 to driving anabolism, the high $NADPH/NADP^+$ ratio provided a driving force for the glutathione reductase
256 reaction with ΔG= −30±7 kJ/mol (**Fig. 6i**). The conserved cellular energetics and thermodynamics across
257 the three T cell types revealed T cells' readiness for increased energy demand and oxidative stress.

Discussion

Our knowledge of adaptive immunity builds on a strong foundation of cellular and molecular interactions between immune cells, receptors, cytokines, antigens, and antibodies as well as the ensuing signaling cascades. What powers these biochemical processes? How can immune cells invariably perform such critical tasks in varying environments? Does human immune diversity manifest in metabolism? The present work complements the growing body of knowledge in immunology by providing the first ever quantitative profiling of the human T cell metabolome in absolute terms.

The governing equations of life mathematically describe, at the local level, the kinetics and thermodynamics of biochemical reactions, and at the systems level, the laws of conservation of mass and energy. Absolute metabolite concentrations are integral elements of the governing equations. Since analytical instruments have varying sensitivities and responses to disparate analytes, however, absolute metabolome quantitation has remained an onerous task that requires large sample sizes. In particular, absolute metabolite concentrations in primary cells and tissues have been inaccessible due to low availability of biological materials. To solve this problem, we developed the ensemble method for quantifying absolute metabolite concentrations *en masse*.

With our ensemble quantitation method in hand, we quantified absolute metabolite concentrations in human T cells for the first time. T cell metabolism underlies adaptive immunity by supplying cellular energy and biochemical building blocks for activation, differentiation, and proliferation[7-10] as well as production of cytokines and cytotoxic granules[16,45-48]. Thus, knowledge of absolute concentrations provides a quantitative and mechanistic understanding of T cell metabolism and establishes a solid foundation for promoting immunity[49,50] and developing immunotherapy for cancer[14,51-53] and autoimmune diseases[32,54-56].

A key finding from our ensemble quantitation in human primary T cells is the conservation of metabolome across subtypes and individuals. Between five individuals and their helper ($CD4^+$) and killer ($CD8^+$) T cells, the lowest R^2 observed was 0.8. Despite helper and killer T cells carrying out distinct functions in the adaptive immune system, their basal metabolic profiles resemble each other and indicate energy and redox homeostasis. On the one hand, the high metabolic similarity across individuals implies that metabolic variability may not stand in the way of allogeneic immunotherapy. On the other hand, ensemble absolute metabolome quantitation across a larger number of individuals may reveal the unique metabolic features of a "super donor," whose cells would lead to successful treatment of many patients. Our data provides a baseline for healthy T cell metabolism, opening the door to biomarker discovery.

The observed conservation of metabolite concentrations manifests a metabolic design principle: cells prioritize concentration homeostasis despite a high turnover of metabolites. How can metabolites exert control of metabolic activity without a substantial change in concentrations? In reactions that are reversible or moderately forward driven, small changes in metabolite concentrations lead to large changes in reaction rates[21,57]. Furthermore, since each metabolite is involved in multiple reactions and pathways as substrates, products and effectors, a substantial change in a single metabolite's concentration may have multiple unintended consequences throughout metabolism[58]. Therefore, small variations across multiple metabolites, rather than large variations of few metabolites, may better exert precise pathway-level modulation of metabolic activity. Caution should be exercised, however, not to misconstrue the overall similarity as lack of unique metabolic features.

298 The most notable difference between primary and immortalized T cells was the abundance of aspartate. In
299 primary T cells, aspartate is the most abundant metabolite at 35-39 mM, whereas in Jurkat cells it just
300 makes the top ten with 6.9 mM. Besides protein synthesis, aspartate serves three important functions: i)
301 electron translocation from the cytosol to the mitochondrial matrix as part of the malate-aspartate shuttle;
302 ii) biosynthesis of asparagine and nucleotides; and iii) anaplerosis. In T cells, both aspartate and asparagine
303 have been linked to stress response pathways and effector function. Aspartate deficiency is a biomarker of
304 autoimmune T cells from rheumatoid arthritis patients[32]. Aspartate deficiency lowers NAD^+/NADH and
305 ADP-ribosylation of GRP78/BiP, a regulator of endoplasmic reticulum (ER) stress, causing the expansion of
306 ER membrane and the biogenesis of a proinflammatory cytokine tumor necrosis factor (TNF). Aspartate
307 supplementation was sufficient to recover healthy T cell function. Asparagine availability and asparagine
308 synthetase (ASNS) activity modulate T cell metabolism, effector function, and antitumor response[59-61]. The
309 immunometabolite itaconate decreases $CD8^+$ T cell proliferation in part by reducing aspartate, glycine and
310 serine biosynthesis flux in $CD8^+$ T cells[33]. Supplementation with aspartate, glycine and serine or
311 nucleosides restores T cell proliferation, with aspartate supplementation being essential for the anti-tumor
312 effector function of $CD8^+$ T cells. Thus, aspartate is a key regulator of T cell inflammatory response (*cf.*
313 succinate and itaconate in macrophages[62-64]) and we surmise that a high aspartate concentration is a
314 hallmark of healthy T cells.

315 In addition to uncovering the conserved features of T cell metabolism, a key contribution of this work is the
316 ensemble method for absolute metabolome quantitation, which standardizes metabolomics, augments its
317 utility, and engenders kinetic and thermodynamic insights. The ensemble method can be applied to not
318 only suspension cultures but also adherent cell cultures and tissues (**Extended Data Fig. 7**). Knowledge of
319 absolute metabolite concentrations transcends the boundaries of individual metabolomics studies, which
320 cannot be unified due to batch effects, and lays the foundation for cumulative knowledgebase of
321 metabolism. It facilitates the determination of fluxes in non-steady-state conditions[65,66], quantification of
322 organelle-specific metabolites[67], identification of metabolite-protein interactions[68,69], and integration of
323 multi-omic datasets[70]. We envision our ensemble quantitation method being applied to the >400 major cell
324 types in the human body[71] to create an atlas of human metabolome. The resulting knowledge will serve as a
325 conduit for connecting biochemistry to mathematical modeling, advance predictive biology, and reveal
326 master regulators of metabolism.

Methods

Negative selection of CD4+ and CD8+ T cells

CD4+ and CD8+ primary T cells were isolated from peripheral blood mononuclear cells (PBMCs) of healthy donors by magnetic-activated cell sorting (MACS). PBMCs were isolated from healthy donor blood (courtesy of the UCLA Blood and Platelet Center) by density gradient centrifugation using Ficoll-Paque PLUS (Cytiva) (courtesy of the UCLA Virology Core Laboratory). To prevent unintended metabolic reprogramming due to the binding of antibodies to the surface antigens of T cells[14,72], negative selection strategies for CD4+ and CD8+ were employed. Manufacturer protocols for CD4+ and CD8+ negative selection kits (Miltenyi Biotec) were followed. PBMCs were spun down, rinsed with PBS, and resuspended in PBS containing 0.5% BSA and 2 mM EDTA (Miltenyi Biotec) at a concentration of 40 μL buffer per 10^7 cells. Biotin-conjugated antibody cocktail (Miltenyi Biotec) was added at 10 μL per 10^7 cells, and the cells were incubated for 5 minutes in the refrigerator (2-8°C). After allowing antibodies to bind to cognate antigens, 30 μL of buffer per 10^7 cells was added along with 20 μL of MicroBead Cocktail (Miltenyi Biotec) per 10^7, and the cells were incubated for 10 minutes in the refrigerator (2-8°C). For negative selection of CD4+ T cells, biotin-conjugated antibody cocktail included antibodies against CD8, CD14, CD15, CD16, CD19, CD36, CD56, CD123, TCR γ/δ, and CD235a (Glycophorin A), and MicroBead Cocktail included MicroBeads conjugated to anti-biotin antibody and anti-CD61 antibody to remove CD8+ T cells, monocytes, neutrophils, eosinophils, B cells, dendritic cells, NK cells, granulocytes, γ/δ T cells, erythroid cells, megakaryocytes, and platelets. For negative selection of CD8+ T cells, biotin-conjugated antibody cocktail included antibodies against CD4, CD15, CD16, CD19, CD34, CD36, CD56, CD123, TCRγ/δ, and CD235a (Glycophorin A), and MicroBead Cocktail included MicroBeads conjugated to anti-biotin antibody, anti-CD14 antibody, and anti-CD61 antibody to remove CD4+ T cells, monocytes, neutrophils, eosinophils, B cells, stem cells, dendritic cells, NK cells, granulocytes, γ/δ T cells, erythroid cells, megakaryocytes, and platelets.

LS columns (Miltenyi Biotec) were rinsed with buffer, and then the cells were added to the columns. The initial flow through represented the enriched CD4+ or CD8+ population. Once isolated, the cells were spun down at 200g for 10 minutes, the supernatant was decanted, and the cells were resuspended in RPMI supplemented with 10% dialyzed fetal bovine serum (dFBS). CD4+ or CD8+ T cells were incubated at 37°C and 5% CO_2 for 1-2 hours before extraction. For amino acid measurement, cells from Donor E and Donor F were cultured for two hours in standard RPMI 1640 media diluted threefold with amino acid deprived RPMI media supplemented with 10% dFBS.

Population purity was verified with flow cytometry (**Extended Data Fig. 8**). To confirm the purity of isolated CD4+ and CD8+ T cells from PBMCs, cells were stained with the following antibodies: CD3 (APC, clone REA613, Miltenyi Biotec), CD4 (VioBlue, clone REA623, Miltenyi Biotec), and CD8 (FITC, clone REA715, Miltenyi Biotec). A suspension of 5×10^5 cells in 100 μL of PBS containing 0.5% BSA and 2 mM EDTA was prepared. After 2 μL of each antibody solution was added, the cells were incubated on a shaker at room temperature in the dark for 10 minutes, washed with 1 mL of buffer, centrifuged at 300g for 5 minutes, and resuspended to a volume of 0.5 mL of staining buffer. Samples were moved to a flow cytometry tube and stored cold (2-8°C) in the dark until transport. Unstained and fluorescence minus one (FMO) control samples were prepared similarly. Single color controls were prepared following the same protocol with positive and negative compensation beads (Miltenyi Biotec) with the same concentration of

367 antibodies added (2 μL antibody solution per 100 μL PBS containing 0.5% BSA and 2 mM EDTA. Cells were
368 analyzed using an LSRFortessa flow cytometer (BD Biosciences), and data were gated and analyzed with
369 Floreada.io.

370 **Cell lines and culture conditions**

371 All cells were cultured in nutrient replete conditions. Jurkat cells (Jurkat clone E6-1, ATCC) were cultured
372 in RPMI 1640 (Gibco) supplemented with 10% dFBS at 37°C and 5% CO_2. For Jurkat cells, partial media
373 change, replacing one third of the cell-free culture volume, was performed every 24 hours and three hours
374 prior to metabolite extraction. Primary T cells were seeded into RPMI 1640 (Gibco) supplemented with
375 10% dFBS at 37°C after negative selection, and their intracellular metabolites were extracted within one to
376 two hours. The cells designated for intracellular amino acid quantification and from Donor E were seeded
377 into a medium with one-third diluted amino acids but otherwise identical to RPMI 1640 supplemented
378 with 10% dFBS. *E. coli* strain NCM3722 was grown in Gutnick minimal medium[73] containing 2 g/L [U-$^{13}C_6$]
379 glucose and 10 mM NH_4Cl at 37°C. *E. coli* cells were cultured in the ^{13}C-labeled medium starting from the
380 inoculation of overnight cultures. Cells were reinoculated from the overnight culture into beveled flasks
381 and grown for four to five hours to the mid-exponential phase before metabolite extraction. *BAX*$^{-/-}$/*BAK*$^{-/-}$
382 immortalized baby mouse kidney (iBMK) cells[74] cells were cultured in DMEM without glucose, pyruvate,
383 and glutamine (Gibco) supplemented with 4.5 g/L [U-$^{13}C_6$] glucose, 584 mg/L [U-$^{13}C_5$] glutamine (99%,
384 Cambridge Isotope Laboratories) and 10% dFBS in six-centimeter plates at 37°C and 5% CO_2 for 72 hours.
385 Fresh medium was replenished every 24 hours and three hours (2 g/L [U-$^{13}C_6$] glucose but otherwise the
386 same medium) prior to metabolite extraction.

387 **Co-extraction of metabolites from two cell types**

388 Jurkat, *E. coli*, and iBMK cells were all extracted when they were exponentially growing. Jurkat cells were
389 extracted when culture density was between 1×10^6 cells/mL to 3×10^6 cells/mL. *E. coli* cells were extracted
390 in the mid-exponential phase at OD_{600} between 0.3 and 0.6. iBMK cells were extracted when cultures
391 reached 60-80% confluence. Primary T cells were extracted one to two hours after isolation from PBMCs,
392 after incubating in RPMI 1640 + 10% dFBS. Viability and growth of mammalian cells were measured by
393 mixing cell suspension with Trypan Blue at a 1:1 ratio and using the Countess II FL Cell Counter (Thermo).

394 For co-extraction of T cells and *E. coli* cells, the two cultures were simultaneously vacuum filtered by
395 pipetting them onto distinct regions of a 47-mm nylon membrane (0.20-μm pore size). Care was taken to
396 ensure that the two cultures did not come in contact. We employed three quenching-extraction methods
397 tailored to redox cofactors, metabolites present in the extracellular space (e.g., amino acids and pyruvate),
398 and all others including central carbon metabolites (**Extended Data Fig. 9a**). Once the cells were separated
399 from the media, the filter was placed cell-side down onto a 6-cm plate containing 1 mL of pre-cooled (–
400 20°C) 40:40:20 LC-MS grade methanol/acetonitrile/water. Extraction continued in a –20°C freezer for 15-
401 20 minutes. The filter was flipped so that the cell side was facing up. The extract solution was mixed well,
402 transferred to an Eppendorf tube, and spun down at 17,000g and 4°C for 10 minutes. For measuring
403 NAD(P)(H), an acidic extraction solvent containing 0.1 M formic acid was used[75] to quench residual
404 enzymatic activity and dissociates metabolites by fully denaturing enzymes, and prior to centrifugation, the
405 extract was neutralized with 15% NH_4HCO_3 (**Extended Data Fig. 9b**). The supernatant was dried under

406 nitrogen gas and reconstituted in LC-MS-grade water for LC-MS analysis. The formic acid extraction
407 enabled the quantification of NADPH and NADH in a reproducible manner (**Extended Data Fig. 9c**).

408 Measurement of intracellular amino acids in T cells required rapidly washing cells to minimize the
409 perturbation of cellular metabolism. Initially, two washing methods, in which 150 mM ammonium acetate
410 at pH 7.4 or PBS (Corning) was pipetted onto cells on nylon filter immediately after vacuum filtration, were
411 tested; however, both led to cell lysis and loss of intracellular metabolites (**Extended Data Fig. 9d**).
412 Instead, a combination of centrifugation and vacuum filtration was used for rapid washing and extraction. T
413 cells were first separated from media by centrifuging 1 mL of culture at 500g for 2 minutes. The
414 supernatant was removed, and cells were resuspended in 1 mL of amino acid-free RPMI 1640 before rapid
415 vacuum filtration and co-extraction as described above (**Extended Data Fig. 9e**). One wash step was
416 sufficient to quickly remove extracellular amino acids (**Extended Data Fig. 9f**). For Jurkat cells, which
417 secreted substantial amounts of pyruvate, pyruvate measurement also followed rapid washing and
418 extraction steps as with amino acids.

419 For co-extraction of T cells and iBMK cells, both culture plates were removed from the incubator
420 simultaneously. Media was aspirated from the iBMK culture plate, extraction solvent was placed on it, the
421 plate was placed on a cold plate. Jurkat cell culture was vacuum filtered on a nylon filter membrane, and the
422 filter was placed onto the iBMK extraction plate with the cell side facing down onto the extraction solvent
423 (**Extended Data Fig. 7a**). The plate was placed in the –20°C freezer for 15-20 minutes. The adherent cells
424 were detached using a cell lifter, the filter was flipped cell-side up, and the extract solution was mixed well.
425 The metabolite extract was collected, spun down at 17,000g and 4°C for 10 minutes. The supernatant was
426 dried under nitrogen gas and reconstituted in LC-MS-grade water for LC-MS analysis.

427 **Metabolite measurement**

428 The metabolite extracts were analyzed by LC-MS, a Vanquish Duo UHPLC (Thermo) coupled to a Q Exactive
429 Plus mass spectrometer (Thermo). The LC separation was achieved using a hydrophilic interaction
430 chromatography column (XBridge BEH Amide Column, 130 Å, 2.5 µm, 2.1 mm × 150 mm, Waters). The A
431 and B solvents were 95:5 water/acetonitrile with 20 mM ammonium acetate, 39 mM ammonium hydroxide
432 (pH 9.4) and 99:1 acetonitrile/water, and the gradient was the same as previously reported[14,76]. MS was
433 performed in positive and negative ion mode with a mass resolution of 140,000 at 200 *m/z* (mass-to-
434 charge ratios). LC-MS data were processed using the Metabolomic Analysis and Visualization Engine
435 (MAVEN)[77]. The m/z values from monoisotopic masses and the retention times from authenticated
436 standards were used to identify peaks. For isomers glucose-6-phosphate and fructose-6-phosphate, which
437 were not separated by the LC method, the ratio of isomers in the cells of interest was assumed to be the
438 same as in the reference cells, and a single peak and U/L ratio were taken for both isomers. For arginine
439 and glycine, whose concentrations could not be reliably obtained from co-extraction, known concentrations
440 of arginine and glycine standards were spiked into cellular extracts, and cellular arginine and glycine
441 concentrations were computed using the increase in the ion counts relative to the unspiked aliquots and
442 the ion counts in the unspiked aliquots. A previously reported concentration value for dTTP concentration
443 in *E. coli* was inaccurate. To measure the correct absolute concentration of dTTP in *E. coli*, *E. coli* strain
444 NCM3722 was grown in Gutnick minimal medium[73] containing 2 g/L [U-$^{13}C_6$] glucose and 10 mM NH_4Cl at
445 37°C , and metabolites were extracted using 40:40:20 methanol/acetonitrile/water containing a known

amount of unlabeled dTTP. The samples were prepared and analyzed as described above, and the new dTTP concentration was calculated from the ratio of unlabeled to labeled dTTP. The new dTTP concentration in *E. coli* was 1.81×10^{-4} M with the 95% confidence interval [1.54×10^{-4} M, 2.13×10^{-4} M]. Using this new reference concentration, dTTP concentrations in T cells were determined using the co-extraction method.

Absolute metabolome quantitation and statistical analysis

Absolute metabolite concentrations were determined by the ratio of unlabeled to ^{13}C-labeled metabolites, the ratio between aqueous cell volumes of cells of interest and reference cells, and the known absolute concentration in the reference cells. Measured U:L ratios depend on the intracellular aqueous volumes (V) and metabolite concentrations ([met]) in each cell type:

$$Measured\ U{:}L\ ratio = \frac{12C\ Ion\ Counts}{13C\ Ion\ Counts} = \frac{V_{COI}\times[met]_{COI}}{V_{REF}\times[met]_{REF}} \qquad \text{... Equation 5}$$

The concentration of each metabolite was calculated by:

$$\ln[met]_{COI} = \ln\frac{U}{L} + \ln\frac{V_{REF}}{V_{COI}} + \ln[met]_{REF} \qquad \text{... Equation 6}$$

Where $[met]_{COI}$ and $[met]_{REF}$ is the metabolite concentration in the cells of interest (COI) and reference cells (REF) , $\frac{U}{L}$ is the ratio of unlabeled ions to labeled ions, V_{COI} and V_{REF} are the aqueous cell volumes of COI and REF. For *E. coli*, culture density (OD_{600}) was measured using a spectrophotometer and converted to aqueous cell volume using the conversion[24]: $1\ OD_{600} = \frac{7\times10^{-16}\ L\ (aqueous\ vol)}{1\ cell}\frac{1\ cell}{3\times10^{-13}\ gCDW}\frac{0.47\ gCDW}{1\ L\ (culture)}$. For primary T cells, Jurkat cells, and iBMK cells, packed cell volume was measured and converted to the aqueous cell volume using the conversion $1\ \mu L\ (PCV) = 0.7\ \mu L\ (aq\ vol)$.

Once metabolites concentrations were determined using **Eqn. 6** for individual samples, average levels and confidence intervals for metabolites were derived by bootstrapping. Since $\frac{U}{L}$ values influenced the accuracy of metabolite concentration measurement (**Fig. 1f**), bootstrapping was carried out by weighting metabolite concentrations based on $\frac{U}{L}$. The weights were derived from the relationship between $\frac{U}{L}$ and the corresponding R^2 values across the metabolome in the co-extraction validation study (**Fig. 1f**).

$$R^2(k) = 1 - \frac{SS_{res}}{SS_{tot}} = 1 - \frac{\sum_i(\log U_i - \log kL_i)^2}{\sum_i(\log U_i - \overline{\log U})^2} \qquad \text{... Equation 7}$$

k represents expected $\frac{U}{L}$ ratio (1, 4, and 20 in the validation study), i represents metabolite index, and U_i and L_i represent ion counts for unlabeled and ^{13}C-labeled metabolite i.

The weights for individual metabolite concentrations in bootstrapping were determined by the likelihood of the measurements given their $\frac{U}{L}$ values accurately capturing the true concentrations, which were represented by R^2. To determine weights for the individual samples whose metabolites were extracted from various $\frac{U}{L}$ values, the known k and R^2 values were fitted to a gaussian curve using nonlinear regression (**Extended Data Fig. 2**). The resulting weight function $w\left(\frac{U}{L}\right)$ was used to determine resampling probabilities for weighted bootstrapping of T cells concentrations measurements.

$$w\left(\frac{U}{L}\right) = a \times e^{-\frac{\left(\ln\frac{U}{L}\right)^2}{2c^2}} \qquad \text{... Equation 8}$$

The values a = 0.831451 and c = 4.575862 were determined by non-linear least squares fitting. Each measured $\frac{U}{L}$ ratio was used to determine a metabolite concentration using **Eqn. 6** and a weight value w_i using **Eqn. 8**. For each metabolite, the probability of selecting a concentration measurement in weighted bootstrapping was computed by dividing its weight by the sum of the weights of all measurements:

$$P(i) = \frac{w_i}{\sum_j w_j} \qquad \text{... Equation 9}$$

For each metabolite, the log-concentration ($\ln[met]_{COI}$) distribution was bootstrapped by resampling 10,000 means, each of which was calculated from n (the number of samples) log-concentration measurements selected according to $P(i)$ with replacement (**Extended Data Fig. 2**). The standard error s_{met} of log concentrations from the bootstrapped distribution was obtained by dividing the range of the 95% confidence interval by 4. However, this error represented a compounding effect of independent random errors from both COI (T cells) and REF cells. The errors for metabolites specifically in COI (T cells) were propagated using the compound standard error s_{met} and the standard error of $[met]_{REF}$ ($s_{[met]_{REF}}$):

$$s_{[met]_{COI}} = \begin{cases} \sqrt{{s_{met}}^2 - {s_{[met]_{REF}}}^2} & {s_{met}}^2 > {s_{[met]_{REF}}}^2 \\ s_{[met]_{REF}} & {s_{met}}^2 \leq {s_{[met]_{REF}}}^2 \end{cases} \qquad \text{... Equation 10}$$

The 95% confidence interval of each metabolite was determined as the mean ± 2 $s_{[met]_{COI}}$ in logarithmic space:

$$\ln[met]_{COI} \in [\overline{\ln[met]_{COI}} - 2s_{[met]_{COI}}, \overline{\ln[met]_{COI}} + 2s_{[met]_{COI}}] \qquad \text{... Equation 11}$$

Metabolome distribution analysis using Zipf's law and genome-scale metabolic model

Metabolite concentrations were randomly sampled from the respective 95% confidence intervals and ranked from the largest to the smallest. Concentrations were log-transformed and used to fit log-transformed Zipf's law:

$$\ln[met]_n = C - \alpha \cdot \ln(n) \qquad \text{... Equation 12}$$

, where n is the rank (with the highest concentration corresponding to n=1), $[met]_n$ is the nth-ranked metabolite concentration, $C \in [\overline{\ln[met]_1} - 2s_{[met]_1}, \overline{\ln[met]_1} + 2s_{[met]_1}]$, and $\alpha \in [0.90\ , 1.10]$. Metabolite concentrations partially followed Zipf's law. Thus, the number of Zipfian metabolites was determined as the largest rank N such that the best-fit line described by **Eqn. 12** for metabolites ranked 1 through N fell within the bounds set for C and α. The random sampling and fitting processes were repeated 10,000 times to find the maximum N. The instance shown in **Fig. 4a** was the first permutation encountered with the maximum N.

The numbers of reactions that individual metabolites are involved with were obtained from Recon3D, a genome-scale reconstruction of human metabolism[31]. For each measured metabolite, all rows of the S matrix of Recon3D corresponding to the metabolite were probed, and all non-zero columns therein

corresponding to reactions (including transport reactions) were counted. This reaction count represented the total number of unique reactions across all compartments.

Michaelis constants (K_m) and inhibitor dissociation constants (K_i)

Absolute metabolite concentrations were compared to known Michaelis constants (K_m) and inhibitor dissociation constants (K_i). K_m and K_i values in *Homo sapiens* were extracted from BRENDA using the Python 3 implementation of the Simple Object Access Protocol (SOAPpy)[78]. Entries corresponding to mutant enzymes were removed. When multiple entries for the same enzyme-metabolite pair were available, K_m or K_i was represented by the geometric mean. The true interquartile range of $\ln([met]/K_m)$ was compared to a distribution of interquartile ranges determined by 1,000 random permutations of K_m values for enzyme active sites. The $\ln([met]/K_m)$ and $\ln([met]/K_i)$ distributions were compared using the Kolmogorov-Smirnov test. The skewness of each distribution was represented by the Fisher-Pearson coefficient of skewness (g_1).

Gibbs free energy of reaction

Gibbs free energies of lumped glycolytic steps and glutathione reductase were calculated using the eQuilibrator API[79] by inputting the measured absolute concentrations of glycolytic intermediates, ATP, ADP, inorganic phosphate, NAD(H), NADP(H), glutathione, and glutathione disulfide. Inorganic phosphate concentration was set to the geometric mean of the range 2.5-5 mM based on the phosphate concentration in RPMI 1640 of 5.6 mM (Gibco) and previous measurements in mammalian cells[80,81]. Intracellular glucose concentration was set to the geometric mean of the range 0.1-6 mM based on previous measurements in mammalian cells[82-84]. For intracellular inorganic phosphate and glucose, the standard errors of their log concentrations were obtained by dividing the reported range in logarithmic space by 4.

Gibbs free energy changes for lumped reactions were calculated when intermediate metabolite concentrations were unknown. Gibbs free energy changes for the following reactions and lumped reactions were calculated.

Hexokinase (HK) reaction:

$$Glucose + ATP \rightarrow G6P + ADP$$

Phosphoglucoisomerase (PGI) reaction:

$$G6P \rightarrow F6P$$

Phosphofructokinase (PFK) reaction:

$$F6P + ATP \rightarrow FBP + ADP$$

Lumped fructose-bisphosphate aldolase (FBA), triosephosphate isomerase (TPI), glyceraldehyde-3-phosphate dehydrogenase (GAPDH), phosphoglycerate kinase (PGK) reactions:

$$FBP + 2\,NAD + 2\,Pi + 2\,ADP \rightarrow 2\,3PG + 2\,NADH + 2\,ATP$$

Lumped phosphoglycerate mutase (PGAM), enolase (ENO) reactions:

$$3PG \rightarrow PEP + H_2O$$

Pyruvate kinase (PYK) reaction:

$$PEP + ADP \rightarrow PYR + ATP$$

Overall glycolysis:

$$Glucose + 2\,NAD + 2\,ADP + 2\,Pi \rightarrow 2\,PYR + 2\,NADH + 2\,ATP + 2\,H_2O$$

Glutathione reductase:

$$NADPH + GSSG + H^+ \rightarrow NADP^+ + 2\,GSH$$

The error for each (lumped) reaction step was calculated by error propagation with the standard errors of the standard Gibbs free energy and the log concentrations of substrates and products (**Supplementary Table 10**). For instance, the error propagation formula for the Gibbs free energy of a reaction with the form $aA + bB \rightarrow cC + dD$, where lowercase letters represent stoichiometric coefficients for metabolites in capital letters was:

$$s_{\Delta G} = \sqrt{(s_{\Delta G^\circ})^2 + (RT)^2((a \cdot s_{ln[A]})^2 + (b \cdot s_{ln[B]})^2 + (c \cdot s_{ln[C]})^2 + (d \cdot s_{ln[D]})^2)} \quad \text{... Equation 13}$$

559 **Data availability**

560 Source data for all Figures (absolute metabolite concentrations, kinetic constants, and thermodynamic
561 constants) are provided in Supplementary Tables 1-10 and the GitHub public repository:
562 https://github.com/samokeeffe/abs-met-quant

563 **Code availability**

564 The code for bootstrapping and computational analyses is available on the GitHub public repository:
565 https://github.com/samokeeffe/abs-met-quant

566

567 **Acknowledgements**

568 The authors would like to thank the members of the Park lab, the UCLA Molecular Instrumentation Center,
569 the UCLA Metabolomics Center, the UCLA-CDU Center for AIDS Research (CFAR), and the UCLA Flow
570 Cytometry Core for helpful discussion. PBMCs were obtained from the UCLA-CDU CFAR Virology Core Lab
571 that is supported by National Institutes of Health grant number 5P30 AI028697. Flow cytometry was
572 performed in the UCLA Jonsson Comprehensive Cancer Center (JCCC) and Center for AIDS Research Flow
573 Cytometry Core Facility that is supported by National Institutes of Health awards P30 CA016042 and 5P30
574 AI028697 and by the JCCC, the UCLA AIDS Institute, the David Geffen School of Medicine at UCLA, the UCLA
575 Chancellor's Office, and the UCLA Vice Chancellor's Office of Research. This work was supported by the
576 National Institutes of Health under instrumentation grant number 1S10OD016387-01, the National Center
577 for Complementary and Integrative Health of the National Institutes of Health under award number
578 R21AT012814 (J.O.P.), and the National Institute of General Medical Sciences of the National Institutes of
579 Health under award number R35GM143127 (J.O.P.).

580

581 **Contributions**

582 S.O.K. and J.O.P. designed the study and wrote the manuscript. S.O.K., H.S., E.M., and J.O.P. carried out the
583 experiments. S.O.K. and H.S. isolated primary T cells and performed flowcytometry. S.O.K., H.S., E.M., and
584 J.O.P. performed metabolomics analysis.

585 **Figures**

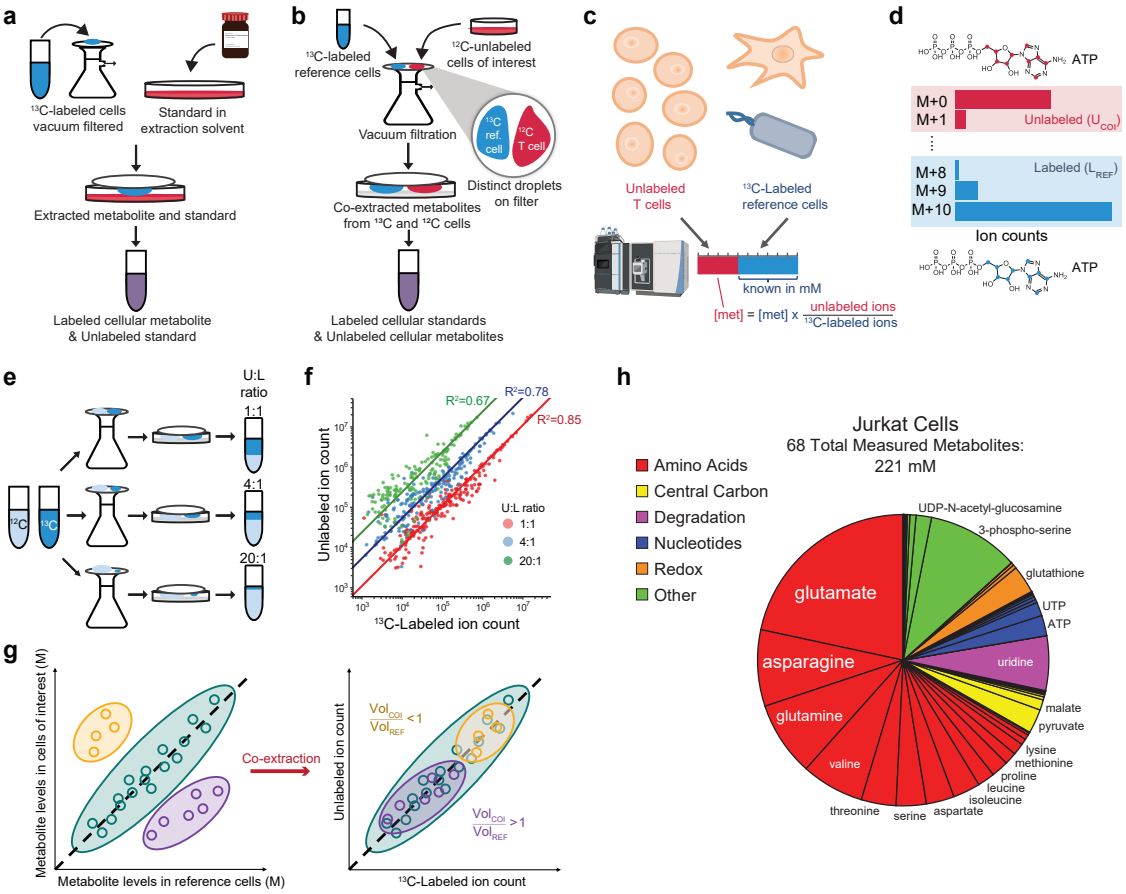

586

587 **Figure 1. Metabolite co-extraction enables ensemble quantitation using ^{13}C-labeled metabolome as**
588 **internal standards.** (**a**) Current absolute metabolite quantitation relies on the use of an authenticated
589 standard dissolved in metabolite extraction solvent. Cells of interest are grown in ^{13}C-labeled media and
590 extracted into the solvent containing the known concentration of the unlabeled standard. (**b**) In the present
591 work, co-extraction of metabolites from two cell types, one of which was ^{13}C-labeled, enabled absolute
592 quantitation of multiple metabolites in parallel. Care was taken to not put the two cell types in contact
593 during co-extraction. (**c**) The resulting LC-MS peaks contained a mixture of unlabeled metabolites from T
594 cells and ^{13}C-labeled metabolites from reference cells. Using the ratios of unlabeled to labeled metabolite
595 peaks and the known concentrations of metabolites in reference cells (blue), absolute metabolite
596 concentrations in T cells were obtained. (**d**) For each metabolite that has n carbons, multiple mass
597 isotopomers with monoisotopic masses from M+0 (unlabeled) to M+n (fully ^{13}C-labeled) were observed.
598 With natural ^{13}C abundance, isotope impurity, and $^{12}CO_2$ incorporation metabolic pathways in mind, each
599 mass isotopomer was attributed to either the cell of interest (COI) or the reference cell (REF). (**e**) This
600 ensemble method was tested by co-extracting unlabeled and ^{13}C-labeled *E. coli* at the ratios of 1:1, 4:1 and
601 20:1. (**f**) The accuracy of the method was validated by comparing the measured ratios of the unlabeled (U)
602 to labeled (L) ion counts to the expected U:L ratios (n=3 biological replicates for each ratio) for individual
603 metabolites. (**g**) Cell density and extraction volumes were tuned to achieve U:L ratios near 1:1 to minimize
604 measurement errors. (**h**) Upon co-extractions with ^{13}C-labeled *E. coli* and iBMK cells, Jurkat T cell
605 metabolites were quantified using the ensemble method.

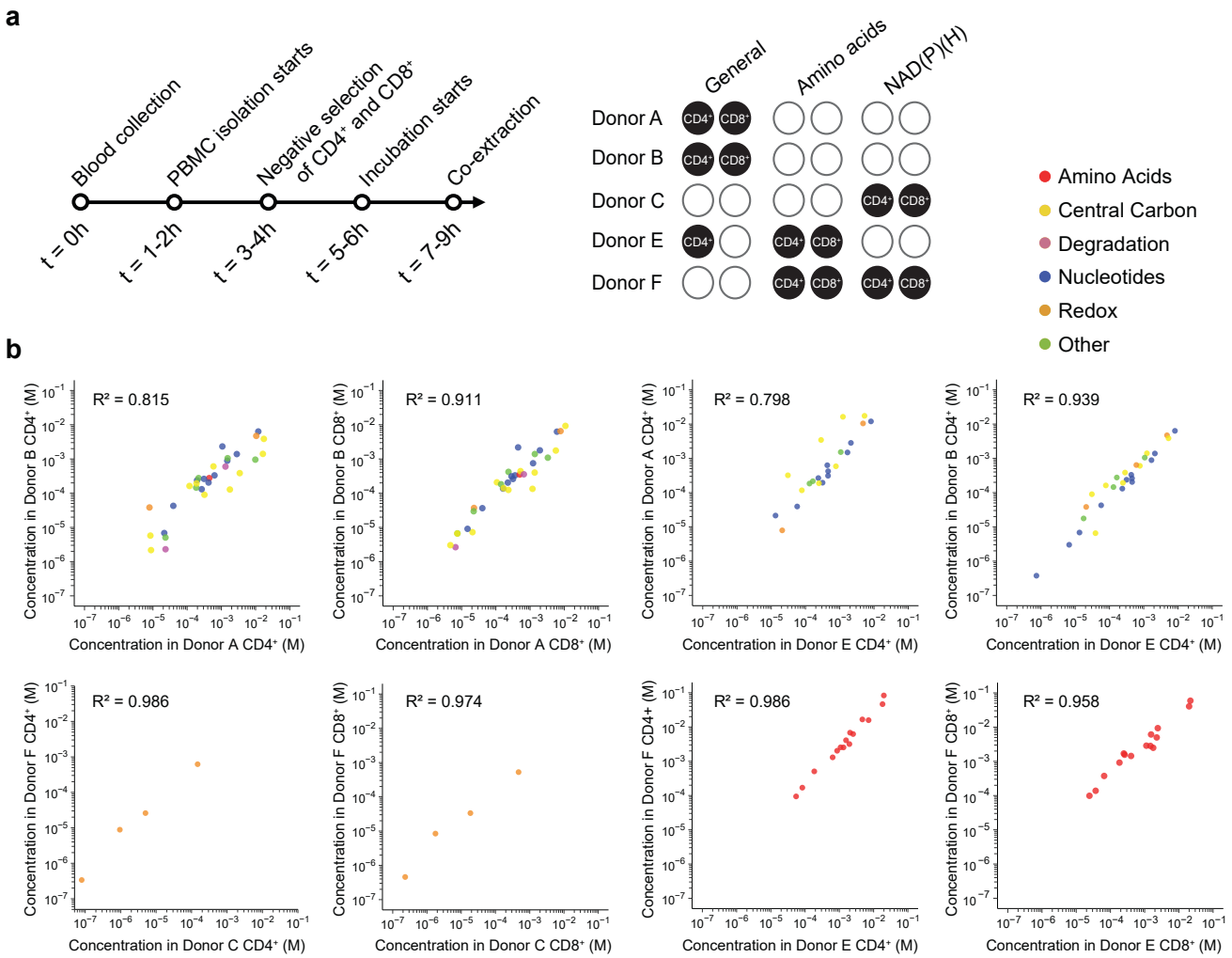

Figure 2. T cell metabolite concentrations are conserved across individuals. (**a**) Primary T cell metabolites were quenched and extracted within 7-9 hours of blood collection from five healthy donors. Different metabolite classes, which required different extraction methods, were measured for each donor because there were not enough T cells to measure all metabolite classes from any one individual. General metabolites included those in central carbon metabolism, degradation pathways, nucleotides and their biosynthesis pathways as well as some redox metabolites (e.g., glutathione) and others. (**b**) Absolute metabolite concentrations were quantified in CD4+ helper T cells and CD8+ killer T cells and were compared across donors.

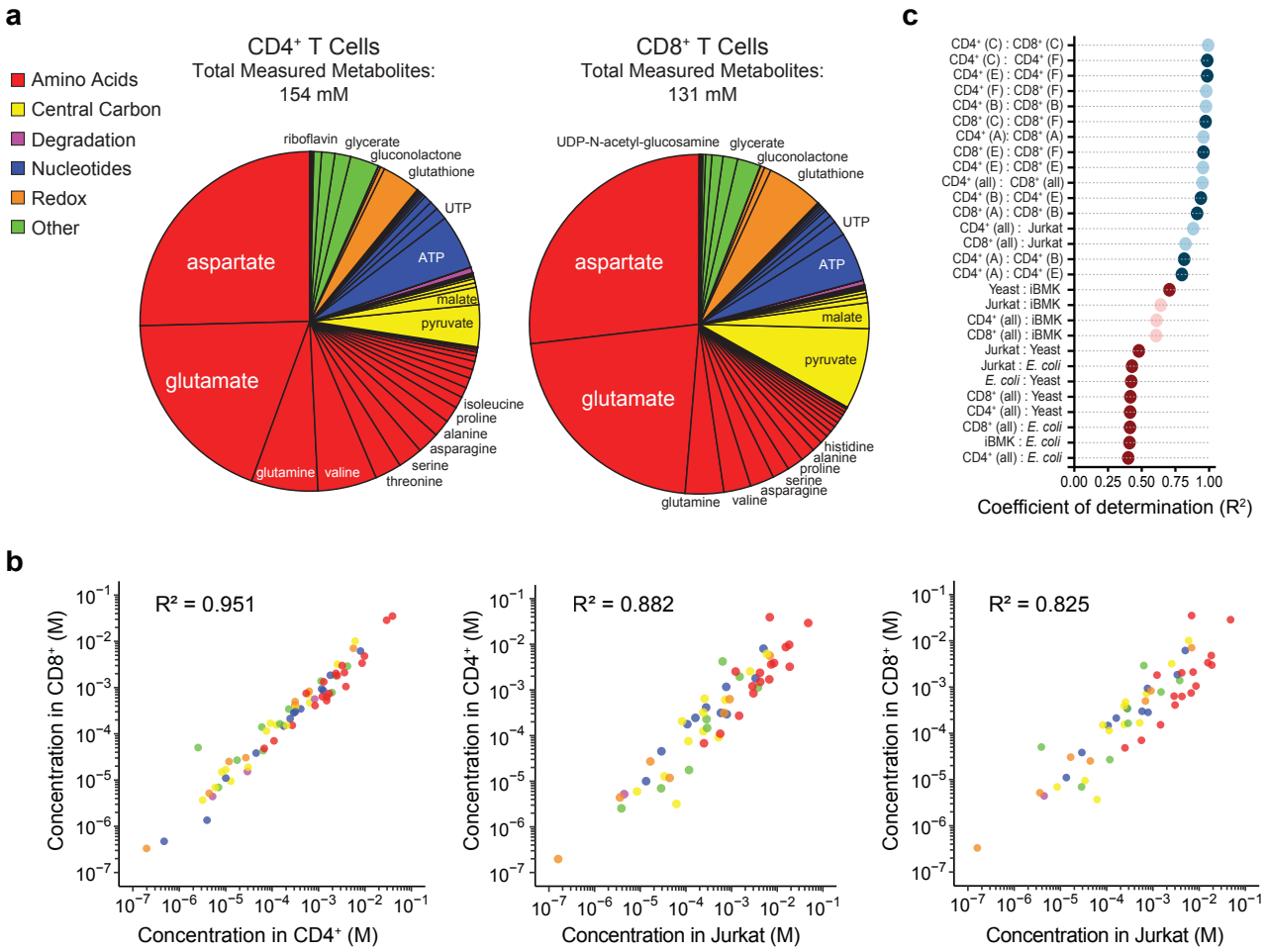

Figure 3. T cell metabolite concentrations are conserved across subtypes. (**a**) Absolute metabolite concentrations in primary T cells were unified in accordance with measurements from all experiments and individuals by bootstrapping (see **Methods**). (**b**) Metabolite concentrations were compared between primary CD4+ and CD8+ T cells and between primary and Jurkat T cells. (**c**) The metabolomes of T cell subtypes from different individuals, *E. coli*, yeast, iBMK, and Jurkat cells were compared. Light blue dots represent comparisons between T cell subtypes; dark blue dots between individuals; light red dots, between T cells and other mammalian cells; and dark red dots, between T cells and microorganisms.

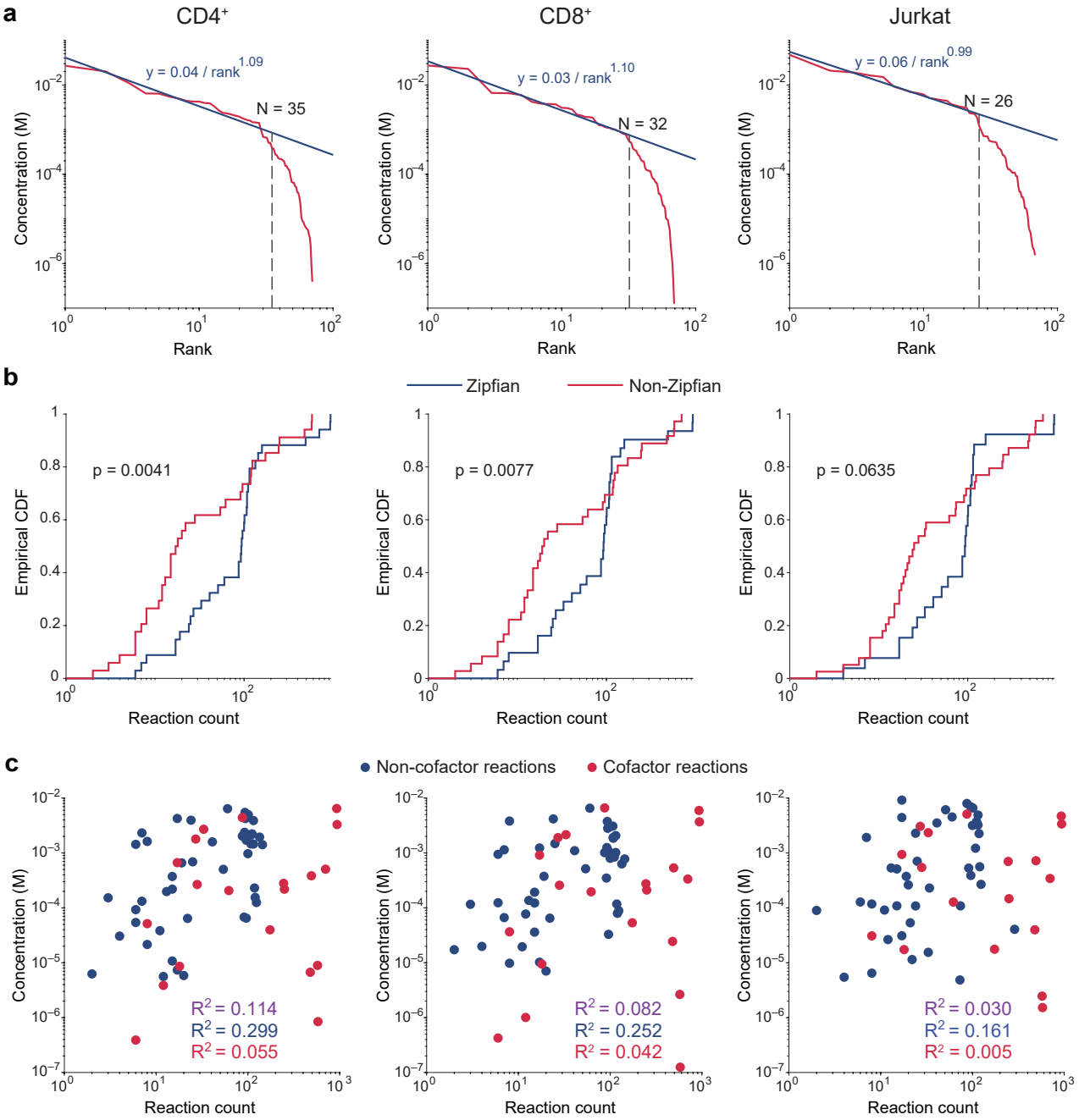

Figure 4. Top metabolites follow Zipf's law and show high connectivity in metabolic networks. (**a**) Metabolite concentrations were rank-ordered from the highest to the lowest, and a line in accordance with Zipf's law was fitted so that it goes through the maximum numbers (N) of metabolites' 95% confidence intervals as possible. (**b**) The cumulative distribution function of total reaction counts associated with individual Zipfian (blue, rank≤N) and non-Zipfian (red, rank>N) metabolites. P values were computed from the Kolmogorov-Smirnov test comparing the two distributions within each T cell type. (**c**) The relationship between metabolite concentrations and connectivities (i.e., the numbers of reactions that individual metabolites participate in) was examined for non-cofactor metabolites (blue), cofactors (red), and all measured metabolites (blue+red=purple).

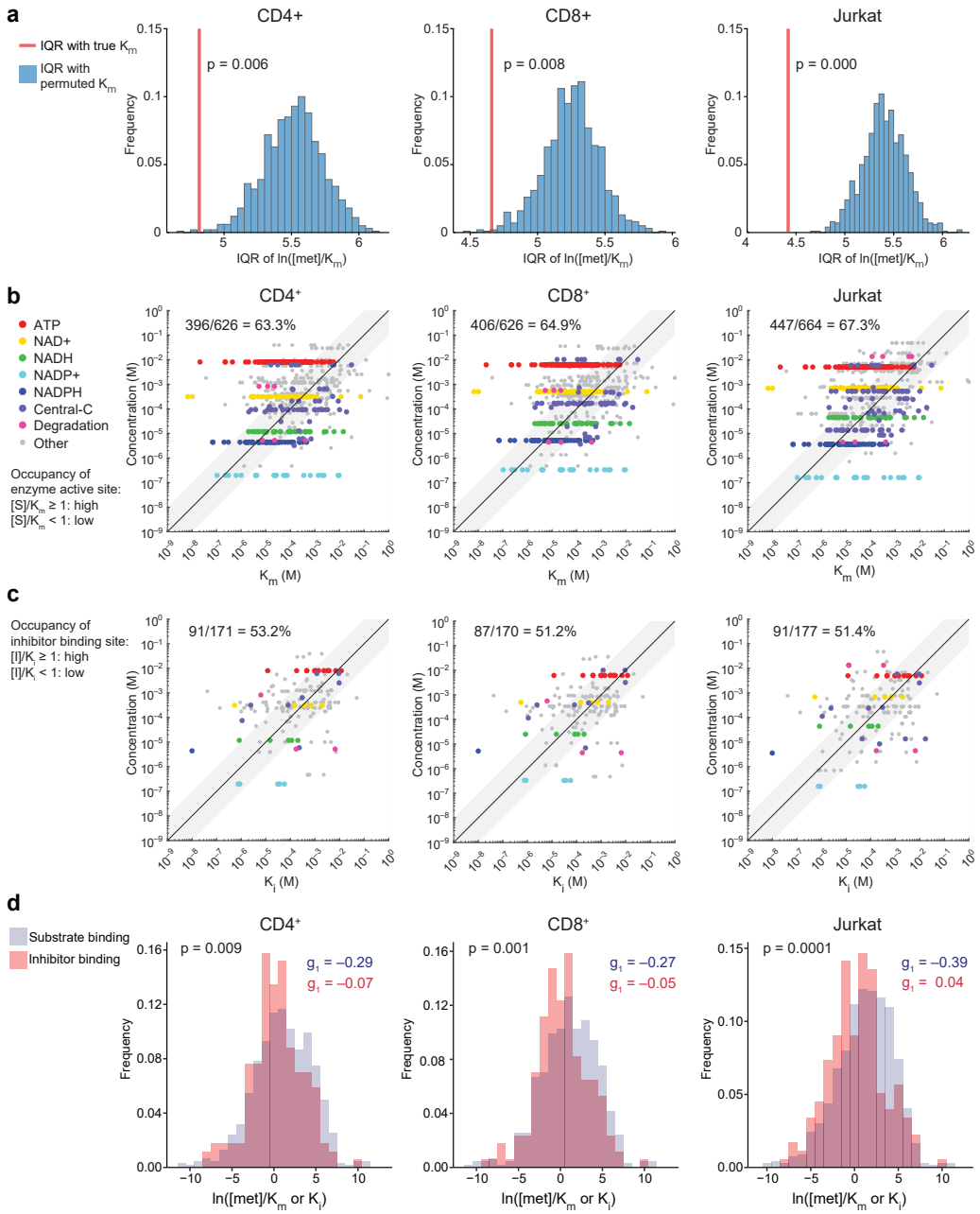

Figure 5. Absolute metabolite concentrations reveal efficient enzyme use. (**a**) The interquartile range (IQR) of ln([met]/K_m) (red line) is significantly lower than that of ln([met]/$K_{m,permuted}$), in which K_m values for enzyme active sites were randomly permuted. P value was twice the fraction of the IQRs with permuted K_m that were less than or equal to the IQR with true K_m. (**b**) Absolute metabolite concentrations were compared with K_m for the associated enzyme active sites. The fraction of concentrations exceeding K_m is shown. (**c**) Absolute metabolite concentrations were compared with inhibitor dissociation constants (K_i) for the associated inhibitor binding sites. The fraction of concentrations exceeding K_i is shown. (**d**) Tendencies for substrate-enzyme binding and inhibitor-enzyme binding were compared across T cell types. P values were from the Kolmogorov-Smirnov test comparing the distributions of ln([met]/K_m) and ln([met]/K_i). The g_1 values represent the Fisher-Pearson moment coefficient of skewness.

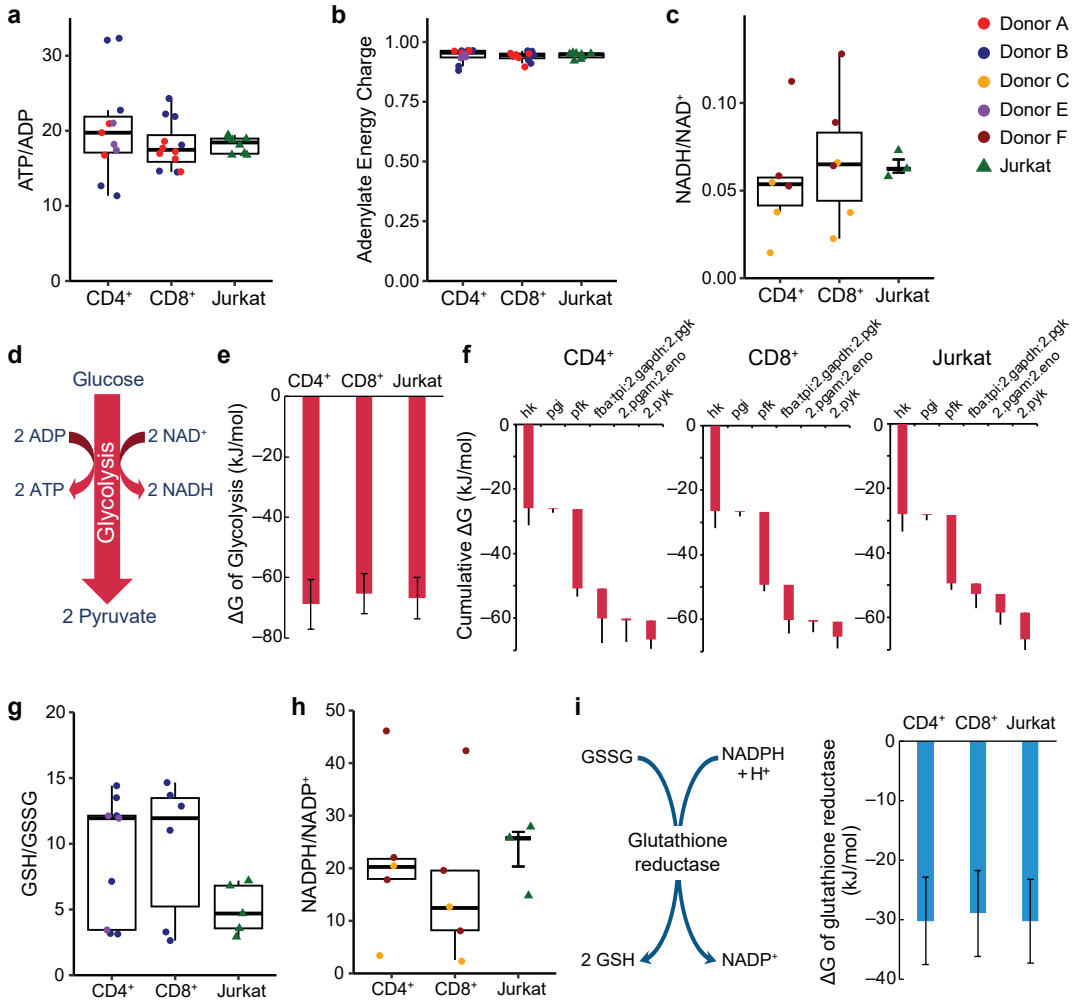

Figure 6. Energetics of T cell metabolism. (**a**) The ratio of ATP to ADP concentrations was calculated for primary CD4+ and CD8+ T cells and Jurkat cells. (**b**) The adenylate energy charge was calculated using the concentrations of ATP, ADP, and AMP. n=11 replicates derived from three donors for CD4+; n=12 replicates derived from two donors for CD8+ T cells; and n=8 replicates for Jurkat cells. (**c**) The ratio of NADH to NAD+ was calculated. n=6 replicates derived from two donors for CD4+ and CD8+ T cells; and n=3 replicates for Jurkat cells. (**d**) Glycolysis converts each molecule of glucose into two molecules of pyruvate while generating two ATP and two NADH. (**e**) Overall Gibbs free energy change across glycolysis in T cells was computed using the net reaction of glycolysis. (**f**) Using the absolute concentrations of glycolytic intermediates, stepwise and cumulative Gibbs free energy changes across glycolysis were computed. (**g**) The ratio of glutathione (GSH) to glutathione disulfide (GSSG) was calculated. n=9 replicates derived from two donors for CD4+ T cells; n=6 replicates derived from a single donor for CD8+ T cells; and n=5 replicates for Jurkat cells. (**h**) The ratio of NADPH to NADP+ was calculated. n=5 replicates derived from two donors for CD4+ and CD8+ T cells; and n=3 replicates for Jurkat cells. (**i**) Glutathione reductase generates reduced glutathione using the reducing power of NADPH. Gibbs free energy of glutathione reductase reaction was computed using substrate and product concentrations. Error bars represent the 95% confidence intervals. Boxplots show the quartiles with thick lines representing the median. The whiskers extend to the farthest measurement values within 1.5 times the IQR from the edges of the box.

663 **Extended Data Figures**

664

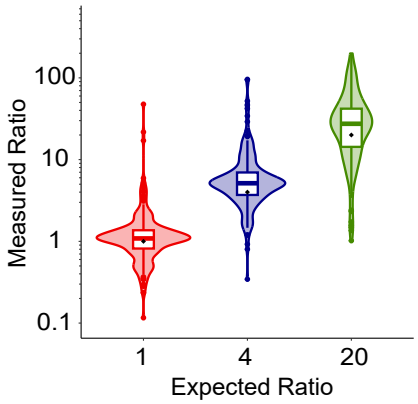

665

666

667 **Extended Data Figure 1. Co-extraction across ranges of metabolite ratios.** The measured ratios of
668 unlabeled (^{12}C) to ^{13}C-labeled metabolites from unlabeled and labeled *E. coli* cultures co-extracted at the
669 ratios of 1:1, 4:1 and 20:1 were compared to the expected ratios (black diamonds).

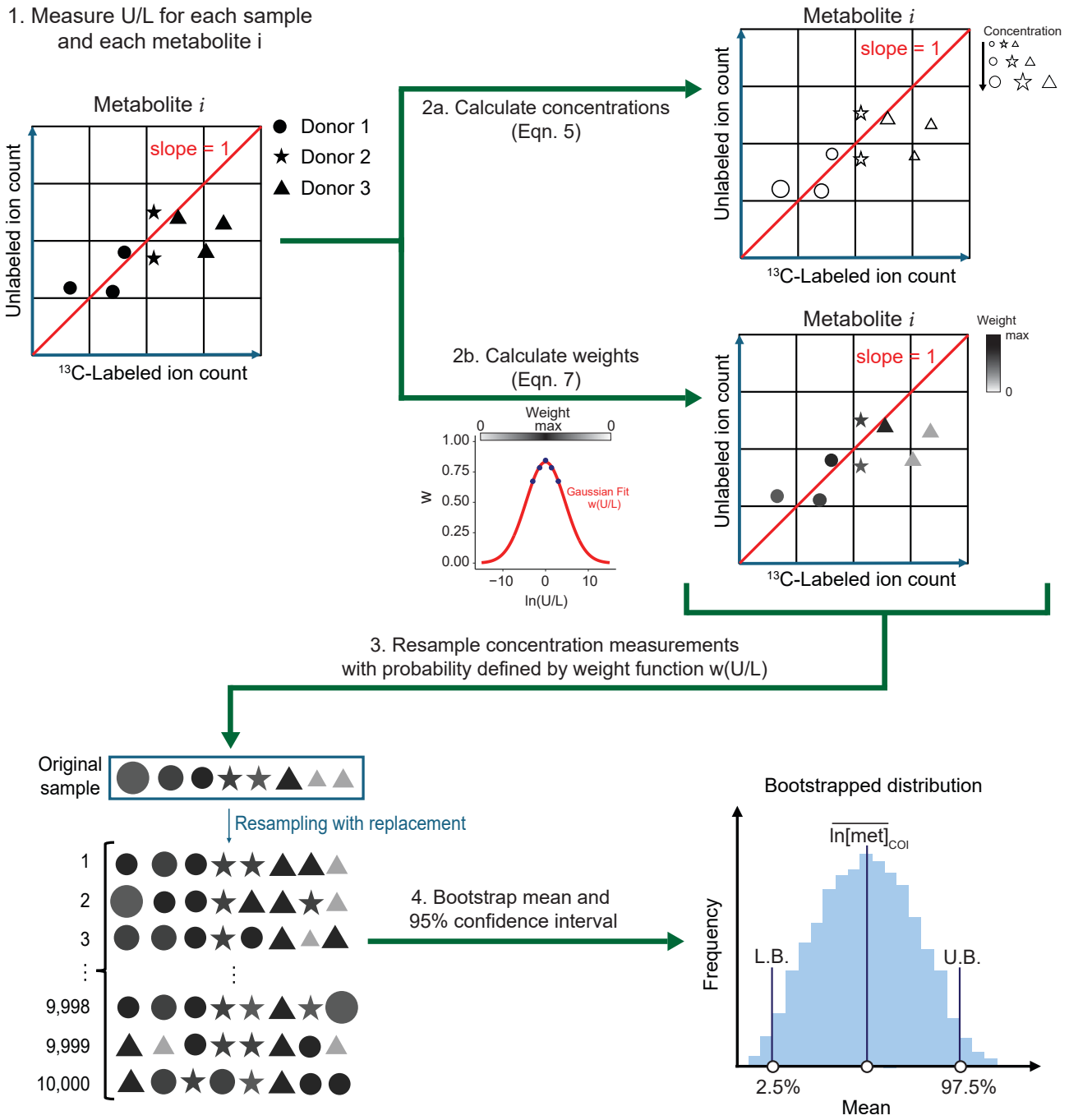

Extended Data Figure 2. Determination of the distribution of log-concentrations of metabolites by bootstrapping. To unify metabolite measurements from multiple experiments and individuals and to determine the mean and 95% confidence interval of each metabolite concentration, a weighted bootstrapping approach was employed. The Gaussian fit w(U/L) assigned a weight for resampling each metabolite concentration measurement using its associated U/L value. Log-concentration distributions were bootstrapped by resampling 10,000 means, each of which was calculated from weighted sampling of n (the number of samples) log-concentration measurements with replacement. The upshot was a reference human T cell metabolome.

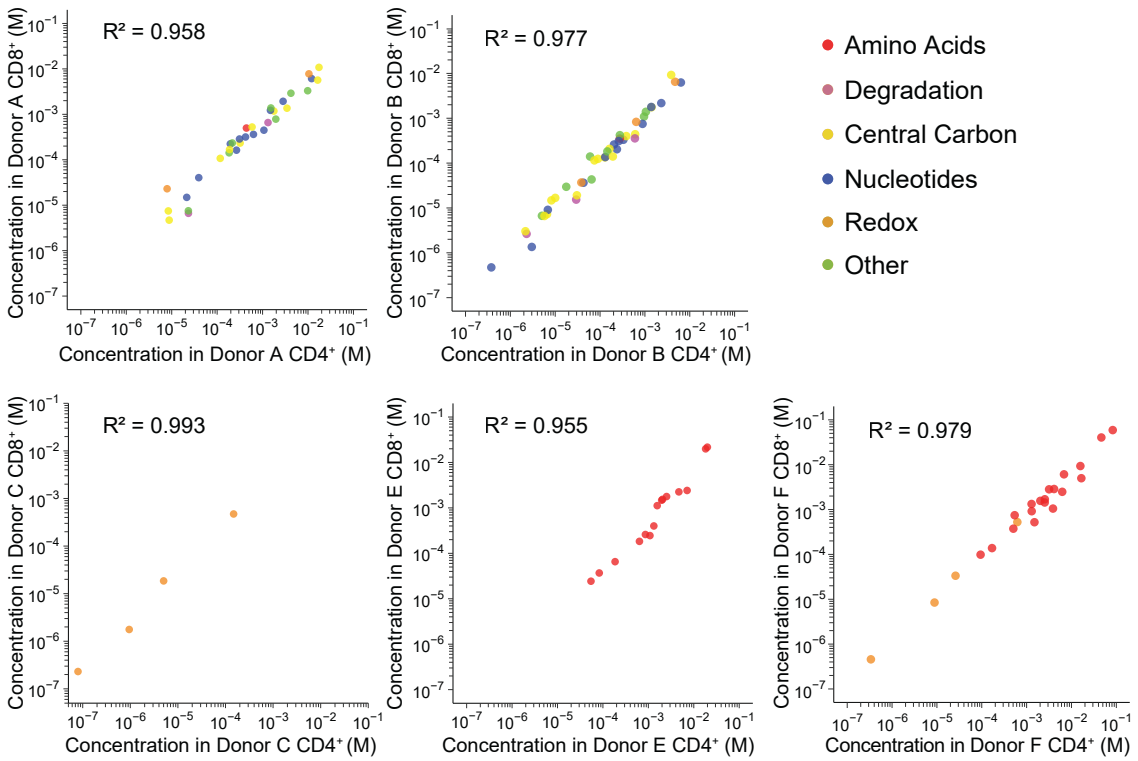

Extended Data Figure 3. Comparison of T cell metabolomes across subtypes from the same individuals. Absolute metabolite concentrations in CD4⁺ helper T cells and CD8⁺ killer T cells from the same individuals were compared.

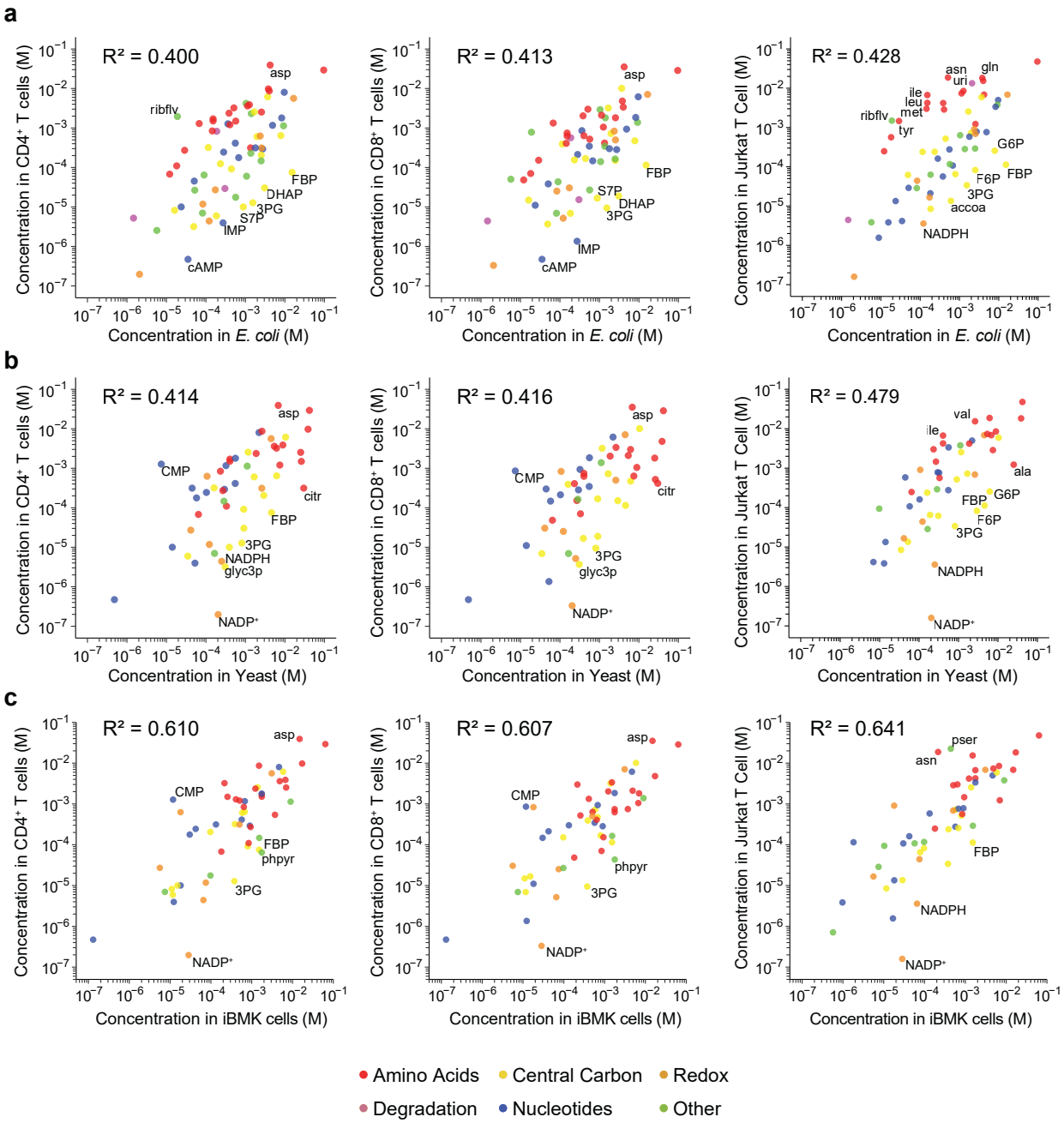

683

684 **Extended Data Figure 4. Comparison of metabolomes between divergent cell types.** (**a-c**) Absolute
685 metabolite concentrations in CD4⁺, CD8⁺ and Jurkat T cells are compared to those of (**a**) *E. coli*, (**b**) yeast,
686 and (**c**) iBMK cells. G6P denotes glucose-6-phosphate; F6P, fructose-6-phosphate; FBP, fructose-1,6-
687 bisphosphate; 3PG, 3-phosphoglycerate; glyc3p, glycerol-3-phosphate; phpyr, phenylpyruvate; citr,
688 citrulline; pser, phosphoserine; ribflv, riboflavin; uri, uridine; and accoa, acetyl-CoA.

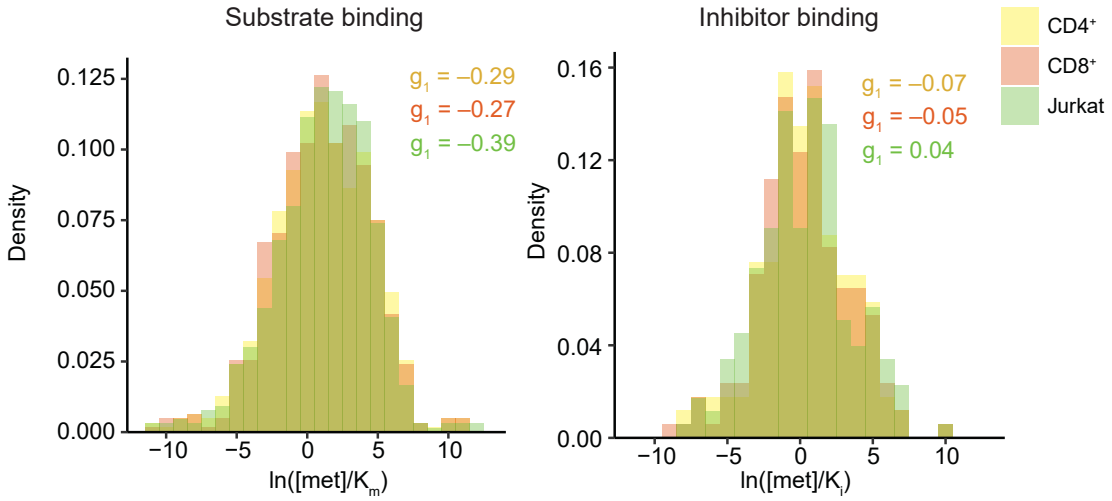

Extended Data Figure 5. Conservation of substrate and inhibitor binding site occupancy across T cell types. The Kolmogorov-Smirnov test on log ratios of metabolite concentrations to K_m and K_i concluded no significant differences between T cell types. g_1 represents the Fisher-Pearson moment coefficient of skewness for CD4+ (yellow), CD8+ (red), and Jurkat (green) T cells.

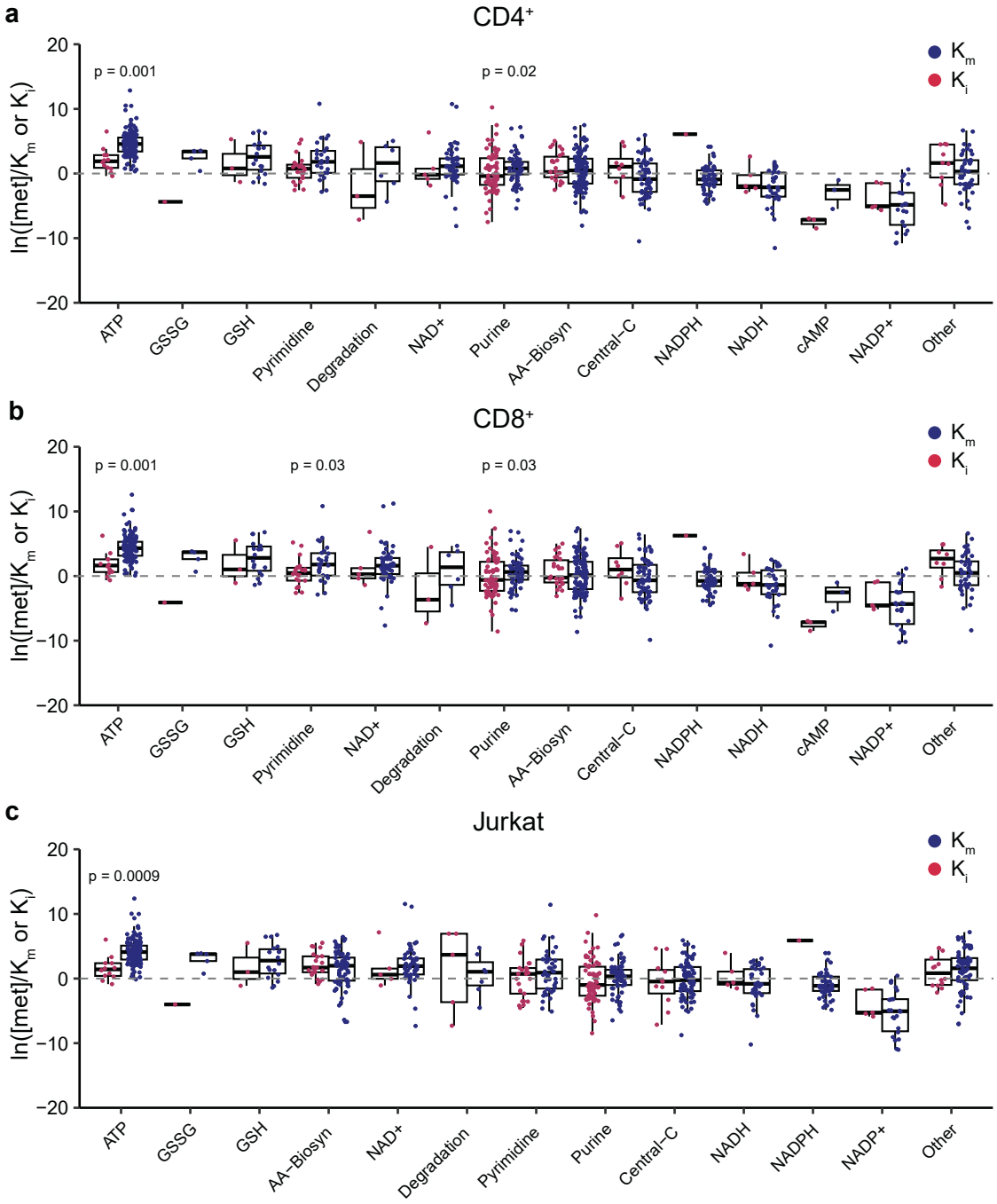

Extended Data Figure 6. Comparison of substrate and inhibitor binding site occupancy across metabolite groups. (**a-c**) Substrate and inhibitor binding site occupancies were compared for individual metabolite groups in (**a**) CD4+, (**b**) CD8+, and (**c**) Jurkat T cells. Boxplots show the quartiles with thick lines representing the median. The whiskers extend to the farthest measurement values within 1.5 times the IQR from the edges of the box. Statistical significance between substrate and inhibitor binding site occupancies for each metabolite group was assessed by the Kolmogorov-Smirnov test and multiple comparison correction using the Benjamini-Hochberg procedure.

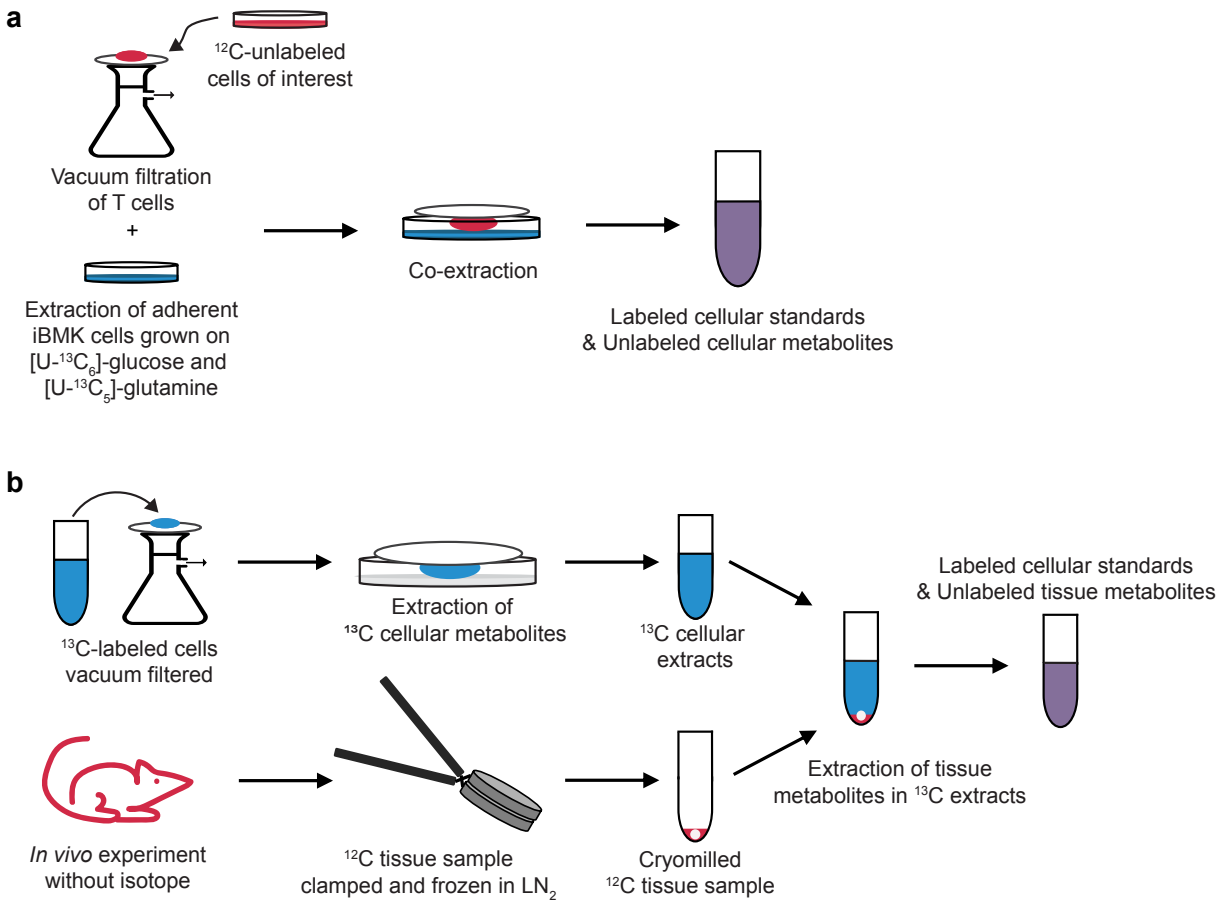

Extended Data Figure 7. Metabolite co-extraction methods for adherent cells and tissues. (**a**) Adherent cells (e.g., iBMK cells) are extracted in the plate that they are cultured, and suspension cells (e.g., T cells) are extracted in the same plate after vacuum filtration. (**b**) Tissues are clamped, snap frozen in liquid nitrogen (LN_2), and cryomilled before metabolite extraction using the extracts of ^{13}C-labeled reference cells.

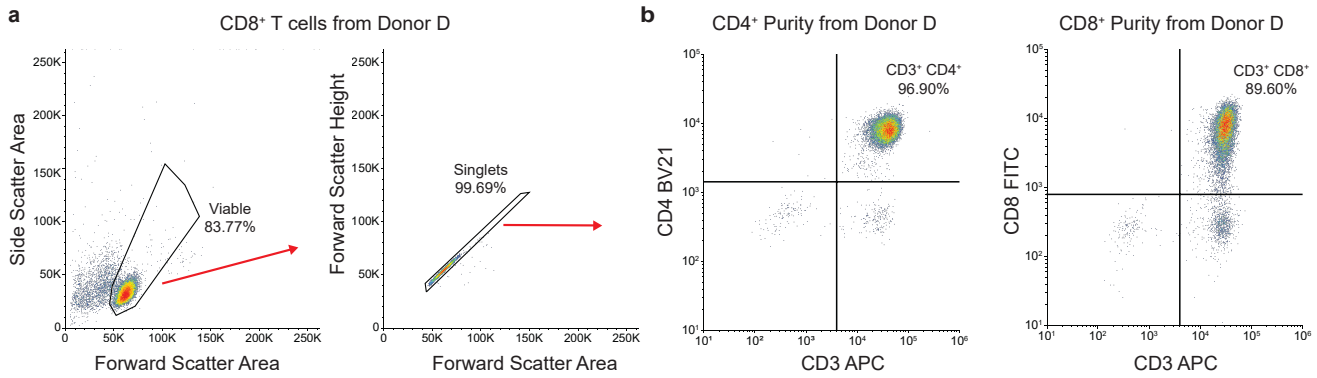

Extended Data Figure 8. Gating strategy for selecting viable cells and determining their subtypes. (**a**) Initial gating excluded debris by analyzing forward-scatter area (FSC-A) and side-scatter area (SSC-A) parameters. Doublets were then excluded using forward-scatter area (FSC-A) versus forward-scatter height (FSC-H). (**b**) The purity of the cell population was assessed by evaluating the singlets based on the fluorescence intensity of anti-CD4 and anti-CD8 antibody staining in conjunction with anti-CD3 antibody staining.

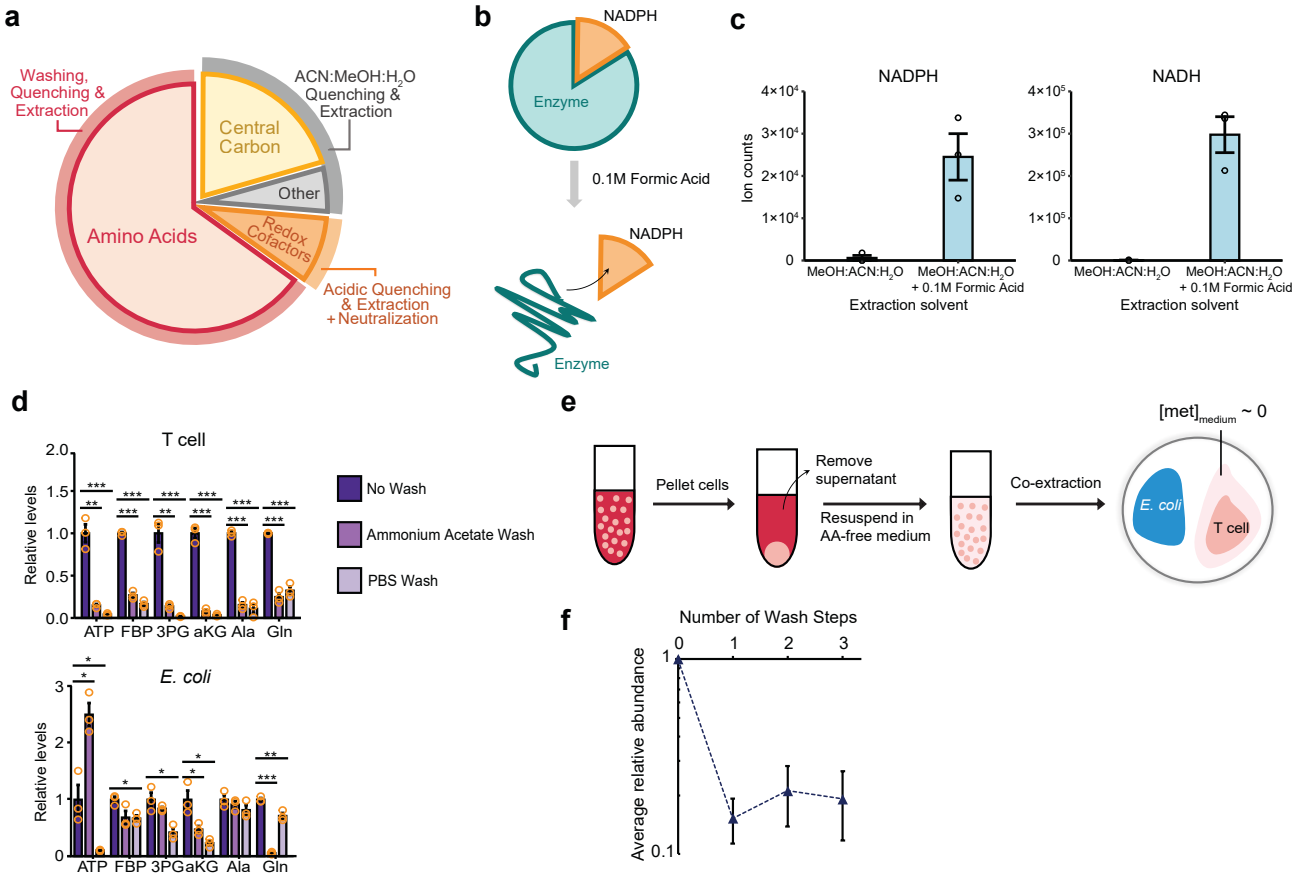

Extended Data Figure 9. Tailored extraction methods capture a broad range of metabolites. (**a**) Three methods for quenching metabolism and extracting metabolite, which were tailored to different metabolite classes, enabled comprehensive metabolite quantitation. (**b**) To extract and measure NAD(P)H, an acidic extraction solvent containing 0.1M formic acid was used to denature enzymes and dissociate them. Acidic extracts were neutralized to prevent the degradation of metabolites. (**c**) Acidic quenching increased ion counts for NADPH and NADH. Error bars represent the s.e.m. (n = 3 biological replicates). (**d**) Relative abundances of representative metabolites were measured with and without washing cells directly on filters. Either 150 mM ammonium acetate (pH 7.4) or PBS was used for washing T cells and *E. coli*. Error bars represent the s.e.m. (n = 3 replicates). P values were calculated using two-tailed t-tests (* represents $p<0.05$, ** represents $p<0.01$, and *** represents $p<0.001$). (**e**) To measure intracellular amino acids without interference from extracellular amino acids, cells were pelleted, supernatant was quickly removed, and cells were resuspended in an amino acid-free medium prior to co-extraction. (**f**) Amino acids were measured after wash steps and compared to the measurement with no wash. The averages of relative amino acid levels are shown with error bars representing the s.e.m. (n = 14 amino acids). A single centrifuge-and-wash step was sufficient to eliminate the interference from extracellular amino acids.

733 **References**

734 1 Biasco, L. *et al.* Clonal expansion of T memory stem cells determines early anti-leukemic responses and
735 long-term CAR T cell persistence in patients. *Nature cancer* **2**, 629-642 (2021).

736 2 Liu, C., Qi, T., Milner, J. J., Lu, Y. & Cao, Y. Speed and location both matter: antigen stimulus dynamics
737 controls CAR-T cell response. *Frontiers in Immunology* **12**, 748768 (2021).

738 3 Acha-Sagredo, A. *et al.* A constitutive interferon-high immunophenotype defines response to
739 immunotherapy in colorectal cancer. *Cancer Cell* **43**, 292-307. e297 (2025).

740 4 Walsh, Z. H. *et al.* Mapping variant effects on anti-tumor hallmarks of primary human T cells with base-
741 editing screens. *Nature biotechnology* **43**, 384-395 (2025).

742 5 Quast, N. P. *et al.* T-cell receptor structures and predictive models reveal comparable alpha and beta
743 chain structural diversity despite differing genetic complexity. *Communications Biology* **8**, 362 (2025).

744 6 Chang, J. T. *et al.* Asymmetric T lymphocyte division in the initiation of adaptive immune responses.
745 *science* **315**, 1687-1691 (2007).

746 7 Macintyre, A. N. *et al.* The glucose transporter Glut1 is selectively essential for CD4 T cell activation and
747 effector function. *Cell metabolism* **20**, 61-72 (2014).

748 8 Zeng, H. *et al.* mTORC1 and mTORC2 kinase signaling and glucose metabolism drive follicular helper T
749 cell differentiation. *Immunity* **45**, 540-554 (2016).

750 9 Michalek, R. D. *et al.* Cutting edge: distinct glycolytic and lipid oxidative metabolic programs are
751 essential for effector and regulatory CD4+ T cell subsets. *The Journal of immunology* **186**, 3299-3303
752 (2011).

753 10 Klein Geltink, R. I. *et al.* Metabolic conditioning of CD8(+) effector T cells for adoptive cell therapy. *Nat*
754 *Metab* **2**, 703-716 (2020).

755 11 Klein Geltink, R. I., Kyle, R. L. & Pearce, E. L. Unraveling the complex interplay between T cell
756 metabolism and function. *Annual review of immunology* **36**, 461-488 (2018).

757 12 Mendoza, A. *et al.* Lymphatic endothelial S1P promotes mitochondrial function and survival in naive T
758 cells. *Nature* **546**, 158-161 (2017).

759 13 Shi, Y., Zhang, H. & Miao, C. Metabolic reprogram and T cell differentiation in inflammation: current
760 evidence and future perspectives. *Cell Death Discovery* **11**, 123 (2025).

761 14 Lakhani, A. *et al.* Extracellular domains of CARs reprogramme T cell metabolism without antigen
762 stimulation. *Nature Metabolism*, 1-18 (2024).

763 15 Wang, R. *et al.* The transcription factor Myc controls metabolic reprogramming upon T lymphocyte
764 activation. *Immunity* **35**, 871-882 (2011).

765 16 Sena, L. A. *et al.* Mitochondria are required for antigen-specific T cell activation through reactive oxygen
766 species signaling. *Immunity* **38**, 225-236 (2013).

767 17 Laniewski, N. G. & Grayson, J. M. Antioxidant treatment reduces expansion and contraction of antigen-
768 specific CD8+ T cells during primary but not secondary viral infection. *Journal of virology* **78**, 11246-
769 11257 (2004).

770 18 Morris, G., Gevezova, M., Sarafian, V. & Maes, M. Redox regulation of the immune response. *Cellular &*
771 *Molecular Immunology* **19**, 1079-1101 (2022).

772 19 Tavassolifar, M. j., Vodjgani, M., Salehi, Z. & Izad, M. The influence of reactive oxygen species in the
773 immune system and pathogenesis of multiple sclerosis. *Autoimmune diseases* **2020**, 5793817 (2020).

774 20 Metallo, C. M. & Vander Heiden, M. G. Understanding metabolic regulation and its influence on cell
775 physiology. *Molecular cell* **49**, 388-398 (2013).
776 21 Park, J. O. *et al.* Near-equilibrium glycolysis supports metabolic homeostasis and energy yield. *Nature*
777 *chemical biology* **15**, 1001-1008 (2019).
778 22 Wegner, A., Meiser, J., Weindl, D. & Hiller, K. How metabolites modulate metabolic flux. *Current opinion*
779 *in biotechnology* **34**, 16-22 (2015).
780 23 Bennett, B. D. *et al.* Absolute metabolite concentrations and implied enzyme active site occupancy in
781 Escherichia coli. *Nature chemical biology* **5**, 593-599 (2009).
782 24 Park, J. O. *et al.* Metabolite concentrations, fluxes and free energies imply efficient enzyme usage. *Nature*
783 *chemical biology* **12**, 482-489 (2016).
784 25 Alseekh, S. *et al.* Mass spectrometry-based metabolomics: a guide for annotation, quantification and
785 best reporting practices. *Nature methods* **18**, 747-756 (2021).
786 26 Guder, J. C., Schramm, T., Sander, T. & Link, H. Time-optimized isotope ratio LC–MS/MS for high-
787 throughput quantification of primary metabolites. *Analytical Chemistry* **89**, 1624-1631 (2017).
788 27 Bennett, B. D., Yuan, J., Kimball, E. H. & Rabinowitz, J. D. Absolute quantitation of intracellular
789 metabolite concentrations by an isotope ratio-based approach. *Nature protocols* **3**, 1299-1311 (2008).
790 28 Ma, E. H. *et al.* Metabolic profiling using stable isotope tracing reveals distinct patterns of glucose
791 utilization by physiologically activated CD8+ T cells. *Immunity* **51**, 856-870. e855 (2019).
792 29 Scherer, S. *et al.* Pyrimidine de novo synthesis inhibition selectively blocks effector but not memory T
793 cell development. *Nature immunology* **24**, 501-515 (2023).
794 30 Mora, T., Walczak, A. M., Bialek, W. & Callan Jr, C. G. Maximum entropy models for antibody diversity.
795 *Proceedings of the National Academy of Sciences* **107**, 5405-5410 (2010).
796 31 Brunk, E. *et al.* Recon3D enables a three-dimensional view of gene variation in human metabolism.
797 *Nature biotechnology* **36**, 272-281 (2018).
798 32 Wu, B. *et al.* Mitochondrial aspartate regulates TNF biogenesis and autoimmune tissue inflammation.
799 *Nature immunology* **22**, 1551-1562 (2021).
800 33 Zhao, H. *et al.* Myeloid-derived itaconate suppresses cytotoxic CD8+ T cells and promotes tumour
801 growth. *Nature metabolism* **4**, 1660-1673 (2022).
802 34 Wang, H. *et al.* Aspartate metabolism facilitates IL-1β production in inflammatory macrophages.
803 *Frontiers in immunology* **12**, 753092 (2021).
804 35 Jha, A. K. *et al.* Network integration of parallel metabolic and transcriptional data reveals metabolic
805 modules that regulate macrophage polarization. *Immunity* **42**, 419-430 (2015).
806 36 Teh, M. R. *et al.* Iron deficiency causes aspartate-sensitive dysfunction in CD8+ T cells. *Nature*
807 *Communications* **16**, 5355 (2025).
808 37 Xia, W., Mao, Y., Xia, Z., Cheng, J. & Jiang, P. Metabolic remodelling produces fumarate via the aspartate–
809 argininosuccinate shunt in macrophages as an antiviral defence. *Nature Microbiology* **10**, 1115-1129
810 (2025).
811 38 Noor, E. *et al.* Pathway thermodynamics highlights kinetic obstacles in central metabolism. *PLoS*
812 *computational biology* **10**, e1003483 (2014).
813 39 Chapman, A. G., Fall, L. & Atkinson, D. E. Adenylate energy charge in Escherichia coli during growth and
814 starvation. *Journal of bacteriology* **108**, 1072-1086 (1971).
815 40 Mak, T. W. *et al.* Glutathione primes T cell metabolism for inflammation. *Immunity* **46**, 675-689 (2017).

816 41 Romeu, M. *et al.* Evaluation of oxidative stress biomarkers in patients with chronic renal failure: a case
817 control study. *BMC research notes* **3**, 1-7 (2010).
818 42 Giustarini, D. *et al.* Pitfalls in the analysis of the physiological antioxidant glutathione (GSH) and its
819 disulfide (GSSG) in biological samples: An elephant in the room. *Journal of Chromatography B* **1019**,
820 21-28 (2016).
821 43 Enns, G. M. *et al.* Degree of glutathione deficiency and redox imbalance depend on subtype of
822 mitochondrial disease and clinical status. *PloS one* **9**, e100001 (2014).
823 44 Valsecchi, F. *et al.* Metabolic consequences of NDUFS4 gene deletion in immortalized mouse embryonic
824 fibroblasts. *Biochimica et Biophysica Acta (BBA)-Bioenergetics* **1817**, 1925-1936 (2012).
825 45 Buck, M. D., O'sullivan, D. & Pearce, E. L. T cell metabolism drives immunity. *Journal of Experimental*
826 *Medicine* **212**, 1345-1360 (2015).
827 46 Buck, M. D. *et al.* Mitochondrial dynamics controls T cell fate through metabolic programming. *Cell* **166**,
828 63-76 (2016).
829 47 Chang, C.-H. *et al.* Posttranscriptional control of T cell effector function by aerobic glycolysis. *Cell* **153**,
830 1239-1251 (2013).
831 48 Greiner, E. F., Guppy, M. & Brand, K. Glucose is essential for proliferation and the glycolytic enzyme
832 induction that provokes a transition to glycolytic energy production. *Journal of Biological Chemistry*
833 **269**, 31484-31490 (1994).
834 49 Pearce, E. L., Poffenberger, M. C., Chang, C.-H. & Jones, R. G. Fueling immunity: insights into metabolism
835 and lymphocyte function. *Science* **342**, 1242454 (2013).
836 50 Reina-Campos, M., Scharping, N. E. & Goldrath, A. W. CD8+ T cell metabolism in infection and cancer.
837 *Nature Reviews Immunology* **21**, 718-738 (2021).
838 51 Kishton, R. J., Sukumar, M. & Restifo, N. P. Metabolic regulation of T cell longevity and function in tumor
839 immunotherapy. *Cell metabolism* **26**, 94-109 (2017).
840 52 Siska, P. J. *et al.* Suppression of Glut1 and glucose metabolism by decreased Akt/mTORC1 signaling
841 drives T cell impairment in B cell leukemia. *The Journal of Immunology* **197**, 2532-2540 (2016).
842 53 Crompton, J. G. *et al.* Akt inhibition enhances expansion of potent tumor-specific lymphocytes with
843 memory cell characteristics. *Cancer research* **75**, 296-305 (2015).
844 54 Franchi, L. *et al.* Inhibiting oxidative phosphorylation in vivo restrains Th17 effector responses and
845 ameliorates murine colitis. *The Journal of Immunology* **198**, 2735-2746 (2017).
846 55 Zhao, Q. *et al.* CD4+ T cell activation and concomitant mTOR metabolic inhibition can ablate microbiota-
847 specific memory cells and prevent colitis. *Science immunology* **5**, eabc6373 (2020).
848 56 Yin, Y. *et al.* (View at Publisher| View at, 2015).
849 57 Hackett, S. R. *et al.* Systems-level analysis of mechanisms regulating yeast metabolic flux. *Science* **354**,
850 aaf2786 (2016).
851 58 Fell, D. & Cornish-Bowden, A. *Understanding the control of metabolism*. Vol. 2 (Portland press London,
852 1997).
853 59 Hope, H. C. *et al.* Coordination of asparagine uptake and asparagine synthetase expression modulates
854 CD8+ T cell activation. *JCI insight* **6**, e137761 (2021).
855 60 Wu, J. *et al.* Asparagine enhances LCK signalling to potentiate CD8+ T-cell activation and anti-tumour
856 responses. *Nature cell biology* **23**, 75-86 (2021).

857 61 Gnanaprakasam, J. R. *et al.* Asparagine restriction enhances CD8+ T cell metabolic fitness and
858 antitumoral functionality through an NRF2-dependent stress response. *Nature Metabolism* **5**, 1423-
859 1439 (2023).
860 62 Mills, E. L. *et al.* Succinate dehydrogenase supports metabolic repurposing of mitochondria to drive
861 inflammatory macrophages. *Cell* **167**, 457-470. e413 (2016).
862 63 Mills, E. L. *et al.* Itaconate is an anti-inflammatory metabolite that activates Nrf2 via alkylation of
863 KEAP1. *Nature* **556**, 113-117 (2018).
864 64 Seim, G. L. *et al.* Two-stage metabolic remodelling in macrophages in response to lipopolysaccharide
865 and interferon-γ stimulation. *Nature metabolism* **1**, 731-742 (2019).
866 65 Young, J. D. INCA: a computational platform for isotopically non-stationary metabolic flux analysis.
867 *Bioinformatics* **30**, 1333-1335 (2014).
868 66 O'Keeffe, S. *et al.* Bringing carbon to life via one-carbon metabolism. *Trends in Biotechnology* (2024).
869 67 Chen, W. W., Freinkman, E., Wang, T., Birsoy, K. & Sabatini, D. M. Absolute quantification of matrix
870 metabolites reveals the dynamics of mitochondrial metabolism. *Cell* **166**, 1324-1337. e1311 (2016).
871 68 Piazza, I. *et al.* A map of protein-metabolite interactions reveals principles of chemical communication.
872 *Cell* **172**, 358-372. e323 (2018).
873 69 Dixit, A. & Kalia, J. Protein-Metabolite Interactions: Discovery and Significance. *ChemBioChem* **24**,
874 e202200755 (2023).
875 70 Kelley, L. P. *et al.* Integrated analysis of transcriptional and metabolic responses to mitochondrial
876 stress. *Cell Reports Methods* **5** (2025).
877 71 Hatton, I. A. *et al.* The human cell count and size distribution. *Proceedings of the National Academy of*
878 *Sciences* **120**, e2303077120 (2023).
879 72 Stanciu, L. A., Shute, J., Holgate, S. T. & Djukanović, R. Production of IL-8 and IL-4 by positively and
880 negatively selected CD4+ and CD8+ human T cells following a four-step cell separation method
881 including magnetic cell sorting (MACS). *Journal of immunological methods* **189**, 107-115 (1996).
882 73 Gutnick, D., Calvo, J. M., Klopotowski, T. & Ames, B. N. Compounds which serve as the sole source of
883 carbon or nitrogen for Salmonella typhimurium LT-2. *Journal of bacteriology* **100**, 215-219 (1969).
884 74 Degenhardt, K. & White, E. A mouse model system to genetically dissect the molecular mechanisms
885 regulating tumorigenesis. *Clinical cancer research* **12**, 5296-5304 (2006).
886 75 Rabinowitz, J. D. & Kimball, E. Acidic acetonitrile for cellular metabolome extraction from Escherichia
887 coli. *Analytical chemistry* **79**, 6167-6173 (2007).
888 76 Wang, L. *et al.* Peak annotation and verification engine for untargeted LC–MS metabolomics. *Analytical*
889 *chemistry* **91**, 1838-1846 (2018).
890 77 Seitzer, P., Bennett, B. & Melamud, E. MAVEN2: an updated open-source mass spectrometry exploration
891 platform. *Metabolites* **12**, 684 (2022).
892 78 Schomburg, I. *et al.* BRENDA in 2013: integrated reactions, kinetic data, enzyme function data,
893 improved disease classification: new options and contents in BRENDA. *Nucleic acids research* **41**,
894 D764-D772 (2012).
895 79 Flamholz, A., Noor, E., Bar-Even, A. & Milo, R. eQuilibrator—the biochemical thermodynamics
896 calculator. *Nucleic acids research* **40**, D770-D775 (2012).
897 80 Xu, H., Yang, D., Jiang, D. & Chen, H.-Y. Phosphate assay kit in one cell for electrochemical detection of
898 intracellular phosphate ions at single cells. *Frontiers in Chemistry* **7**, 360 (2019).

899 81 Bevington, A. *et al.* A study of intracellular orthophosphate concentration in human muscle and
900 erythrocytes by 31P nuclear magnetic resonance spectroscopy and selective chemical assay. *Clinical*
901 *Science* **71**, 729-735 (1986).

902 82 Behjousiar, A., Kontoravdi, C. & Polizzi, K. M. In situ monitoring of intracellular glucose and glutamine in
903 CHO cell culture. *PLoS One* **7**, e34512 (2012).

904 83 Bearham, J., Garnett, J. P., Schroeder, V., Biggart, M. G. & Baines, D. L. Effective glucose metabolism
905 maintains low intracellular glucose in airway epithelial cells after exposure to hyperglycemia.
906 *American Journal of Physiology-Cell Physiology* **317**, C983-C992 (2019).

907 84 Xu, J., Huang, P., Qin, Y., Jiang, D. & Chen, H.-y. Analysis of intracellular glucose at single cells using
908 electrochemiluminescence imaging. *Analytical chemistry* **88**, 4609-4612 (2016).

909